מכון ויצמן למדע

WEIZMANN INSTITUTE OF SCIENCE

Thesis for the degree
Master of Science

Submitted to the Scientific Council of the
Weizmann Institute of Science
Rehovot, Israel

עבודת גמר (תזה) לתואר
מוסמך למדעים

מוגשת למועצה המדעית של
מכון ויצמן למדע
רחובות, ישראל

By
**Yuval Vardi**

מאת
יובל ורדי

# זרם גרר של אלקטרונים וחורים מעוררים אופטית בשתי שכבות בבורות קוונטיים מצומדים

# Coulomb Drag in an Optically Generated Electron-Hole Bilayer

Advisor:
Prof. Israel Bar-Joseph

מנחה:
פרופ' ישראל בר-יוסף

January 2011

שבט תשע"א

# Acknowledgments

I would like to thank all those who helped me to accomplish this research work. First and foremost, I would like to thank my advisor, Prof. Israel Bar-Joseph, who always provided help, guidance and good advice.

Special thanks I owe to Michael Stern for helping me getting into this field, for the enjoyable time working together and the uncountable number of discussions and advices.

I wish to thank our past and present group members: Eyal Cohen-Hoshen, Valery Garmider, Avi Guttman and Dan Mendels, for their assistance, stimulating discussions and for always maintaining a pleasant and enjoyable atmosphere. I thank Prof. Boris Laikhtman for fruitful discussions.

Last but not least, I would like to thank all the staff members of the sub-micron center, and all my classmates here for the great time and lunch breaks during the last couple of years.

# Abstract

In this work we study Coulomb drag in an electron-hole bilayer system, in which current flowing through the electrons layer exerts a frictional force on holes in the other layer. This drag force is due to Coulomb interaction that results in momentum transfer between the two layers. The Coulomb drag technique allows a direct determination of the inter-layer scattering processes.

Traditionally, electron-hole bilayer systems were formed by doped layers, and control over the carriers density was established by applying voltages. This approach requires large layers separation and high voltages.

Here we introduce a new technique that allows the creation of an electron-hole bilayer system with a narrow barrier. The bilayer system is obtained using optically generated electrons and holes which are separated between two coupled quantum wells by applying an electric field. The generated carriers lifetime can be made as long as microseconds, due to the separation, so this quasi-stable system establishes a thermodynamic equilibrium. The narrow barrier between the layers allows recombination, thus enables us to collect photoluminescence and study the carriers states in the system, simultaneously with transport measurements.

Theoretical studies have predicted a power-law dependence of the drag resistivity with respect to the carriers density, and a quadratic dependence on the temperature. Here we show a transition between two regimes. In the high-density regime the drag resistivity indeed decays as a power-law with respect to the density, and is quadratic in the temperature. It agrees with the previous well-established results. In the low-density regime - a regime which have not been studied so far - we present the first observation of an exponential decay of the drag resistivity with respect to the density.

We show that the transition between the exponential and power-law decay of the drag resistivity occurs at a density in which the single-layer resistance approaches the quantum resistance $h/e^2$ and experiences a sudden drop. Simultane-

ously, an appearance of trions in the photoluminescence spectrum is observed. It is consistent with a disorder-related transition.

# Contents

# Chapter 1

# Introduction

Pairing between quasiparticles constituting a Fermi-liquid system leads to some of the most interesting phenomena in condensed matter physics, such as paired atoms in superfluid $^3$He and Cooper pairs of electrons in superconductors. Much interest has recently focused on bilayer semiconductor heterostructures, where two quantum wells are put in close proximity with a high barrier between them, separating the electrons and holes into the two wells. The competition between intra-layer and inter-layer Coulomb interaction (correlation effects) and the possible binding of the electrons and the holes may lead to exotic ground states, collective properties [1, 2], and quantum phase transitions. The study of the inter-layer interaction and correlation may contribute to the understanding of these phenomena.

## 1.1 Coulomb drag in a bilayer system

### 1.1.1 Basic concept

A current flowing in a low-dimensional electron system can exert a frictional force on a similar nearby conducting system. The inter-layer interaction causes a momentum transfer between the two systems. *Coulomb drag* is the case where the momentum exchange results from direct Coulomb scattering between the carriers in the two systems, and enforces them to move in the same direction.

Normally this effect is unobservably small. The reason for this is that bulk three-dimensional metals have an extremely small screening length, of the order of $0.05nm$, so for larger separation between the systems their interaction is negligible. The situation is different for low-dimensional semiconductor heterostructures.

In GaAs the screening length for conduction band electrons in two dimensions is in the order of $5nm$ (for density of $10^{11}cm^{-2}$ and $T < T_F$). Creating a double quantum well structure in which the two two-dimensional electron/hole gases (2DEG/2DHG) are separated by a distance of this order will enable us to observe the effect.

Coulomb drag can be detected as a voltage $V_D$ appearing in one of the layers (drag layer) when current $I$ is driven through the other layer (drive layer), as can be seen in Fig. 1.1. This technique is based on a proposal by Pogrebinskii [3] and later by Price [4].

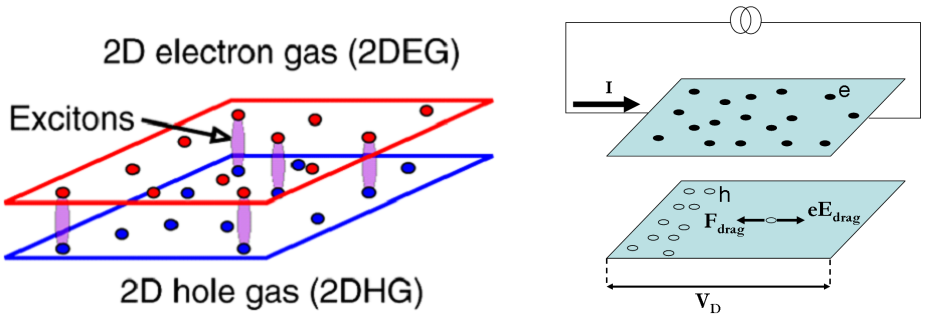


(a) (b)

Figure 1.1: Schematic drawing of the experimental geometry. Electrons and holes are separated between the two layers, current $I$ is driven through one of the layers and drag voltage $V_D$ is induced in the other layer due to the drag force.

The reason for the development of this drag voltage is a momentum exchange between the carriers in the two layers. The carriers in one layer interact with the carriers in the other layer due to the Coulomb potential. The net result of this scattering is that the carriers in the drive layer try to impart their momentum to the carriers in the other layer. Therefore, if we closed the circuit in the drag layer, a small current would actually flow. However, by preventing any current from flowing in the drag layer, a small pile up of charge occurs in one end of the layer which results in a voltage appearing across the drag layer.

Coulomb drag technique allows a unique access to the inter-layer scattering rate via a resistance measurement. This can be simply shown within the Drude model. Taking an electron-hole bilayer, with densities $n, p$ respectively, the equations for

the carriers momentum are:

$$\begin{aligned}\frac{dP_e}{dt} &= -eE_e - m_e v_e \left(\tfrac{1}{\tau_e} + \tfrac{1}{\tau_D}\right) + m_h v_h/\tau_D \\ \frac{dP_h}{dt} &= eE_h - m_h v_h \left(\tfrac{1}{\tau_h} + \tfrac{1}{\tau_D}\right) + m_e v_e/\tau_D \end{aligned} \tag{1.1}$$

where $P_{e,h}, m_{e,h}, v_{e,h}$ are the electron / hole momentum, effective mass and velocity, respectively, $E_{e,h}$ is the electric field in the layers, $\tau_{e,h}$ is the transport intra-layer scattering time, including all momentum relaxation processes except those which transfer momentum between the layers. The inter-layer scattering processes are introduced by the drag relaxation time $\tau_D$. Solving equations (1.1) in steady state one obtains the *resistivity tensor* $\boldsymbol{\rho}$:

$$\begin{pmatrix} E_e \\ E_h \end{pmatrix} = \underbrace{\begin{pmatrix} \frac{m_e}{ne^2}\left(\frac{1}{\tau_e} + \frac{1}{\tau_D}\right) & -\frac{m_h}{pe^2}\frac{1}{\tau_D} \\ -\frac{m_e}{ne^2}\frac{1}{\tau_D} & -\frac{m_h}{pe^2}\left(\frac{1}{\tau_h} + \frac{1}{\tau_D}\right) \end{pmatrix}}_{=\boldsymbol{\rho}} \cdot \begin{pmatrix} J_e \\ J_h \end{pmatrix} \tag{1.2}$$

When current $I$ is driven through one of the layers (e.g. $J_e \neq 0$) and no current flows in the other layer ($J_h = 0$) an electric field (and a voltage $V_D$) develops in the latter layer because of these inter-layer momentum transfer processes. Therefore, we can define the *drag resistivity* as:

$$\rho_D \equiv \frac{V_D}{I}\frac{W}{L} = -\frac{m_e}{ne^2\tau_D} \tag{1.3}$$

where $W, L$ are the width and length of the layers. This expression demonstrates that the drag resistivity $\rho_D$ depends only on the inter-layer momentum relaxation rate, $\tau_D^{-1}$.

It is important to note that the single layer resistivity (diagonal elements in $\boldsymbol{\rho}$) depends on both $\tau_D$ and $\tau_{e,h}$. Since typically the loss of momentum to phonons and impurities is much larger than the loss of momentum to the other layer ($\tau_{e,h} \ll \tau_D$), the drag effect cannot be seen when measuring a single layer resistance. On the other hand, these intra-layer scattering mechanisms (due to disorder, phonons or any other process) do not affect the drag resistivity (off diagonal elements in $\boldsymbol{\rho}$). This is the crucial importance of the Coulomb drag technique. It allows a direct measurement of the inter-layer scattering rate, which would otherwise be completely hidden by the disorder dependent effects ($\tau_e, \tau_h$).

A measure of the relative strength of the disorder scattering and inter-layer Coulomb scattering can be estimated from the ratio of the drag resistivity and the single layer resistivity, which is typically $\rho_D/\rho_{single-layer} < 10^{-3}$.

Also, note that the sign of the drag resistivity reflects the fact that carriers in the drag layer are swept along in the same direction as the carriers in the drive layer are moving.

### 1.1.2 Elementary theory of Coulomb drag

In order to develop a theory for the Coulomb drag, a linearized Boltzmann transport equation for particles in the drag layer is used. This approach was first presented by MacDonald [5] and subsequently by Jauho and Smith [6] with much more details. A detailed calculation was also presented by Rojo [7] and is well explained by Das Gupta [8] and Eisenstein [9]. It results with the following expression for the drag resistivity in an electron-hole bilayer:

$$\begin{aligned} \rho_D &= -\frac{2\hbar^3}{e^2 k_B T n p} \int d\omega \int \frac{d^2\mathbf{q}}{(2\pi)^2} W\left(1,2 \to 1',2'\right) q^2 \\ &\times \int \frac{d^2\mathbf{k_1}}{(2\pi)^2} f_1^0 \left(1 - f_{1'}^0\right) \delta\left(\epsilon_1 - \epsilon_{1'} + \hbar\omega\right) \\ &\times \int \frac{d^2\mathbf{k_2}}{(2\pi)^2} f_2^0 \left(1 - f_{2'}^0\right) \delta\left(\epsilon_2 - \epsilon_{2'} - \hbar\omega\right) \end{aligned} \tag{1.4}$$

where $f^0$ is the equilibrium distribution function, $1,2$ refers to the two layers (primes denote final states), $\mathbf{q} = \mathbf{k_{1'}} - \mathbf{k_1}$, $\epsilon = \frac{\hbar^2\mathbf{k}^2}{2m}$ and $W\left(1,2 \to 1',2'\right)$ is the scattering rate for the process $\mathbf{k_1} + \mathbf{k_2} = \mathbf{k_{1'}} + \mathbf{k_{2'}}$.

Using the Fermi golden rule one gets $W\left(1,2 \to 1',2'\right) = \frac{2\pi}{\hbar} 4 |e\phi(q)|^2$, where $\phi(q)$ is the Fourier transformed screened inter-layer Coulomb interaction (the factor of 4 arises from spin summation and the constraint $\sigma_1 = \sigma_{1'}, \sigma_2 = \sigma_{2'}$). It is convenient to express Eq. (1.4) in terms of the two-dimensional susceptibility function of the free gas $\chi(q,\omega) = -\sum_{\text{spin}} \int \frac{d^2\mathbf{k}}{(2\pi)^2} \frac{f^0(\epsilon) - f^0(\epsilon')}{\epsilon - \epsilon' + \hbar\omega + i\delta}$. This relates to small changes in the density of the 2DEG/2DHG that occur as a result of an external potential.

The expression for the Coulomb drag can be then written in the form:

$$\begin{aligned}\rho_D &= -\frac{\hbar^2}{2\pi^2 e^2 k_B T n p}\int_0^\infty q dq \int_0^\infty d\omega |e\phi(q)|^2 \frac{q^2}{\sinh^2(\hbar\omega/2k_BT)} \\ &\times \; Im(\chi_1(q,\omega))\, Im(\chi_2(q,\omega))\end{aligned} \tag{1.5}$$

It is easy to see that this expression looks very symmetric. It will have the same result when the electrons layer is the drive layer and the holes layer is the drag layer, and in the opposite case. Notice that the opposite case corresponds to simply changing the current and voltage leads of the setup. Indeed, these two configurations should agree, at least in the linear response regime, according to a theorem by Onsager and Casimir [10].

The interaction potential $\phi(q)$, and the degree to which it is screened, is of crucial importance in determining the drag scattering rate. Consider a charge in one of the (infinitely thin) layers. In the absence of screening the potential it produces in the other layer is just $\phi(q) = \frac{e}{2\varepsilon q}\exp(-qd)$, where $d$ is the layers separation. Therefore, drag will be dominated by scattering events with momentum transfers $q < 1/d$. However, when including screening of the charges, both by charges in the same layer and also by charges in the other layer, we get the more complicated potential [11, 6]:

$$\phi(q) = \frac{e}{2\varepsilon}\frac{q\exp(-qd)}{(q+q_s^e)(q+q_s^h) - q_s^e q_s^h \exp(-2qd)} \tag{1.6}$$

where $q_s^{e,h}$ is the screening wave-vector for electrons and holes, respectively. It can be seen that screening reduces the impact of small $q$ processes and so suppresses drag. This implies that for high density the drag resistivity decays. Note that this derivation is for infinitely thin layers. For finite width layers the potential is even more complicated, and can be seen in the references [11, 6].

In general, Eq. (1.5) should be solved numerically. However, for several regimes of the density and temperature an analytic solution can be obtained. Fig. 1.2 shows the dependence of the drag resistivity on the temperature, density and layers separation in these regions, as was calculated by Laikhtman [12]. Appendix A presents the complete results of these calculations.

The most common regime is the low temperatures ($T \ll T_F$) and large interlayer separation ($k_F d \gg 1$, $q_{TF} d \gg 1$ implying a strong screening). Its known

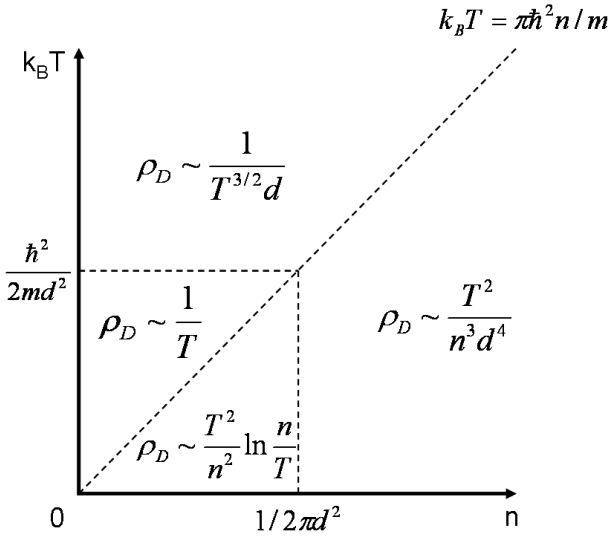


Figure 1.2: Regions of the density $n$ and temperature $T$ where the drag resistivity dependence on these parameters is different, following B. Laikhtman [12]. $d$ is the layers separation.

analytic result is [6]:

$$\rho_D = -\frac{h}{e^2}\frac{\zeta(3)\pi}{32}\frac{(k_BT)^2}{\epsilon_F^e\epsilon_F^h}\frac{1}{(k_F^e d)(k_F^h d)}\frac{1}{(q_{TF}^e d)(q_{TF}^h d)} \tag{1.7}$$

where $\zeta$ is the Riemann zeta function, $q_{TF}^{e,h}$ are the Thomas-Fermi screening wave-vectors, and $\epsilon_F^{e,h}$, $k_F^{e,h}$ are the Fermi energy and wave-vector for the electrons and holes, respectively.

One may notice the $T^2$ dependence. The reason for it is the joint phase space for scattering processes which is dominated by the $k_BT$ thermal smearing of both Fermi surfaces. Also, the $d^{-4}$ scaling of the drag with the layer separation is mainly due to the strong screening effects. Finally, it predicts variation of the drag with density as $n^{-3}$.

### 1.1.3 Experimental results

First we discuss Coulomb drag studies of equal charge bilayer systems. Early Coulomb drag studies were made in bilayer electron systems by Gramila *et al.* [5, 13]. They were performed in a regime of large separation between the layers ($200\mathring{A}$) in which the momentum relaxation rate via virtual phonons was substantial [14]. More recently, Kellogg *et al.* [15] have measured drag in a bilayer electron sam-

ple in which, owing to its smaller layer separation ($100\mathring{A}$) and low density, direct Coulomb scattering dominates the drag at low temperatures. Their results for the drag resistivity agree with a $T^2$ behavior. The coefficient, however, depends on a more sophisticated calculation of the dielectric screening than the simple static Thomas-Fermi screening [16] used in Eq. (1.7). Fig. 1.3a shows the strong effect of the screening model used for the calculation. In addition, corrections due to calculations beyond the random phase approximation include higher order many-body effects on Coulomb drag, especially when the dimensionless parameter $r_s = \frac{E_{e-e}}{E_F} \approx a_B^{-1}(\pi n)^{-1/2}$ grows. Indeed, as can be seen in Fig. 1.3b, the density dependence of the drag was more similar to $n^{-4}$ than to the predicted $n^{-3}$, according to Eq. (1.7). Very similar data also exists for hole-hole bilayer [17, 18].

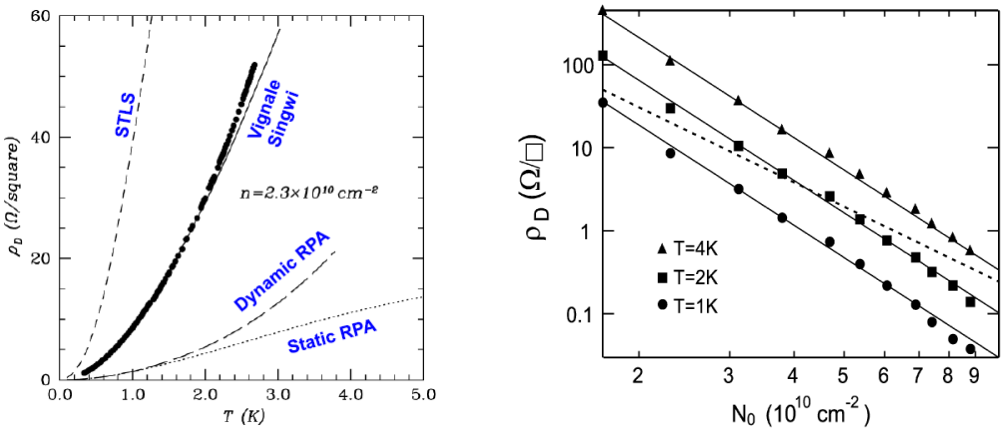


(a) (b)

Figure 1.3: Drag resistivity in an electron-electron bilayer with matched densities, taken from Ref. [15]: (a) Drag resistivity as function of temperature. The solid circles are the experimental data, curves are calculated within several models, see Ref. [16]. (b) Drag resistivity as function of density at $T = 1, 2, 4K$. Solid lines are proportional to $n^{-4}$ while the dashed line is proportional to $n^{-3}$, according to Eq. (1.7).

The study of Coulomb drag in electron-hole bilayer systems reveals some still unresolved questions. The first transport measurement in such systems was made by Sivan *et al.* [19]. Due to the doping, the barrier separating the layers was wide ($200\mathring{A}$) and high enough to prevent tunneling and recombination. The measurement of exciton effects in electron-hole bilayer has proven to be extremely difficult, mostly because of the difficulties associated with fabricating devices with good electrical contacts and small layer separation, but also because of the limi-

tation of adjusting the densities in the two layers to match up the density of the 2DEG to the density of the 2DHG, an issue with significant implications on the drag behavior [20].

A more recent study was done by Seamons *et al.*, using the concept of an undoped electron-hole bilayer (uEHBL) [21]. In these devices the 2DEG and 2DHG were induced using gates that create a strong internal electric field in the heterostructure, and require also a large barrier thickness in order to prevent recombination. Their results agree with the $T^2$ scaling for high temperatures (not with the coefficient). However, they get an upturn in the drag resistivity as the temperature is reduced, see Fig. 1.4a. This anomalous behavior is seen only for the narrower barrier of $200\mathring{A}$ and cannot be seen for $300\mathring{A}$ barrier. Similar anomalous features were also presented by Croxall *et al.* [22, 23]. This upturn in the drag at low temperature cannot be explained within the usual Fermi-liquid theory and may signal the formation of a novel phase in electron-hole system [24]. The origin of this apparent non-Fermi-liquid behavior is still unexplained and requires further theoretical analysis.

Another interesting feature that can be seen in Croxall *et al.* results is that the symmetry between the electrons and the holes in the drag experiments is lacking, see Fig. 1.4b. In the non-$T^2$ region the two measurements of the drag resistivity in the holes and the electrons layer do not agree. This is another puzzling feature, which is not understood at present.

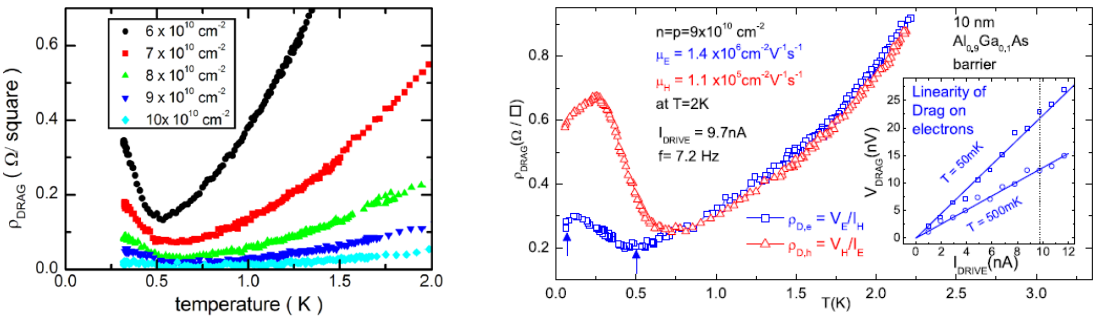


(a) (b)

Figure 1.4: Drag resistivity anomalous in low temperatures in an electron-hole bilayer: (a) Measurement by Seamons *et al.* [21]. An upturn in low temperatures can be seen ($200\mathring{A}$ barrier). (b) Measurement by Croxall *et al.* [22]. In addition to the upturn, the drag resistivity for the electrons and for the holes is different in the low temperature regime, not as expected from a Fermi-liquid behavior.

As can be seen, the deviation from the Fermi-liquid theory is significant at low densities and narrow layer separation (large $r_s$). This regime allows formation of close proximity excitons and strong inter-layer correlations, and may even lead to exotic ground states and condensates [1, 2, 25]. These issues may have a significant effect on the drag resistivity as a measure of the inter-layer scattering processes.

# Chapter 2

# Methods

## 2.1 Excitons in quantum wells

Using molecular beam epitaxy it is possible to grow alternating layers of GaAs and AlGaAs, which form a type I quantum well (QW) in the growth direction (z-direction), due to the different band gap of the two materials. Electrons and holes in this GaAs layer are confined in a one-dimensional potential well. This confinement has a significant effect on the energy states which become discrete in the z-direction, and are functions of the quantum well thickness, the potential width and the effective mass [26].

When GaAs is illuminated with a near band-gap light, electron-hole pairs are created. The Coulomb interaction between the carriers has a significant influence on the electronic states. The attraction between a conduction band electron and a valence band hole gives rise to a bound state called *exciton* [27], which is basically a hydrogenic state. A typical value of the exciton binding energy in a GaAs quantum well is 10 meV.

The system we study is formed by two GaAs quantum wells (QWs), separated by a thin AlGaAs barrier. An external electric field is applied in the z-direction perpendicular to the QWs. Therefore, electrons initially created in one of the wells can tunnel to the second well. This system, of coupled quantum wells (CQWs), enables the formation of spatially indirect excitons. Contrary to direct exciton (X), which is a bound state of an electron and a hole in the same QW, indirect exciton (IX) is a bound state of an electron and a hole in different QWs. Fig. 2.1a illustrates the potential profile along the growth direction and the bound states.

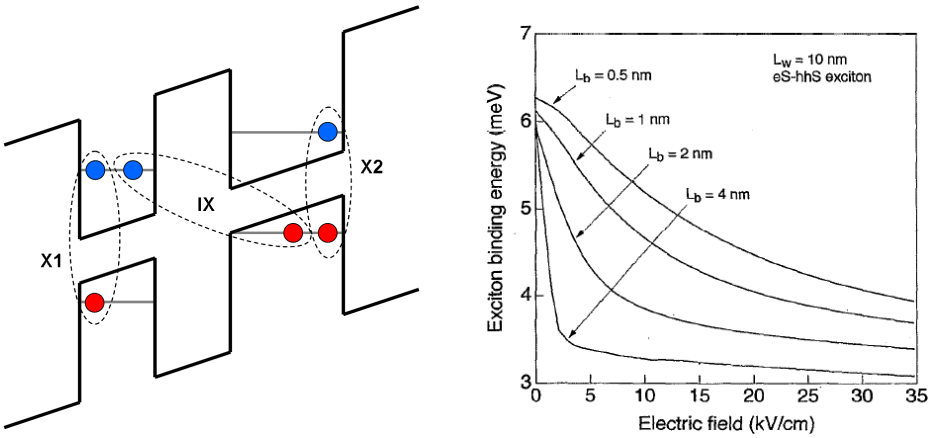


(a) (b)

Figure 2.1: (a) The energy band diagram of asymmetric coupled quantum wells under perpendicular electric field. X1, X2 correspond to direct excitons in the narrow and wide well, respectively, IX corresponds to an indirect exciton. (b) Calculated binding energy for coupled wells of $L_w = 10$ nm, with barrier $L_b$ varied from $0.5 - 4$ nm. After reference [28].

The spatial separation of the electron and the hole into different QWs reduces the IX binding energy. A typical value for the binding energy of IX for the system we discuss is 3 meV, under an applied electric field of 20 kV/cm, as shown in Fig. 2.1b.

## 2.2 Sample design and preparation

The sample that we investigate is an $n^+$-$i$-$n^+$ coupled quantum wells (CQWs) structure grown by molecular beam epitaxy on a semi-insulating GaAs substrate (MBE8-421). The $i$-region consists of two GaAs quantum wells (QWs) of different widths, 7 and 10 nm, separated by a 5 nm $Al_{0.28}GaAs$ barrier. The distance between the two $n^+$ layers is $2.1\mu m$. Using top- and back-gate contacts an electric field is applied in a direction perpendicular to the QWs, such that the electron level in the wide well is higher than that of the narrow well, thus creating a charge separation between the wells. An $100\mu m \times 100\mu m$ mesa was prepared. The schematic of such structure are shown in Fig. 2.2.

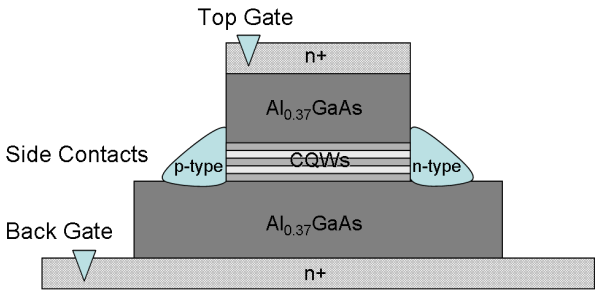


Figure 2.2: Cross section of mesa with the gates the selective side contacts. The CQWs region consists of two GaAs QWs with widths 7, 10 nm (light color), separated by a 5 nm $Al_{0.28}GaAs$ barrier (dark color). An electric field is applied perpendicular to the QWs using the top- and back-gate contacts.

### 2.2.1 Selective ohmic contacts for transport measurements

In order to perform transport measurements of the electrons and holes in the QWs (and drag measurements in particular) ohmic contacts to the QWs are needed to be formed. Furthermore, the ohmic contacts must be selective to either $n$-type or $p$-type carriers (electrons or holes).

The usual procedure for making ohmic contacts to 2DEG/2DHG (depositing a metallic layer on the sample surface and annealing it) has proven to be problematic for intrinsic QWs, in which the carriers are photo-created. The photo-excited carriers do not form a good contact with the annealed region, and a non-linear $I$-$V$ curve is observed [29]. A possible reason for it is shadowing of the region close to the contacts by the metal layers. In order to solve the problem a technique in which the contacts are made to the *sides* of the QWs [30], as seen in Fig. 2.2, has been developed [31]. The annealed region is directly illuminated. A detailed overview of the sample preparation process is presented in Appendix B.

Using this technique, selective $n$-type (Ni/Au/Ge/Au) and $p$-type (Ni/Au/Zn/Au) side contacts [32, 33] connected to the QWs were formed in a geometry shown in Fig. 2.3 (aspect ratio of length/width=0.45). This geometry enables us to perform Coulomb drag measurements as well as single-layer four-probe conductivity measurements (in a mesa in which all side contacts are $n/p$-type). The selectivity of contacts that had been fabricated in this technique was verified by measuring the conductance of 2DEG and 2DHG.

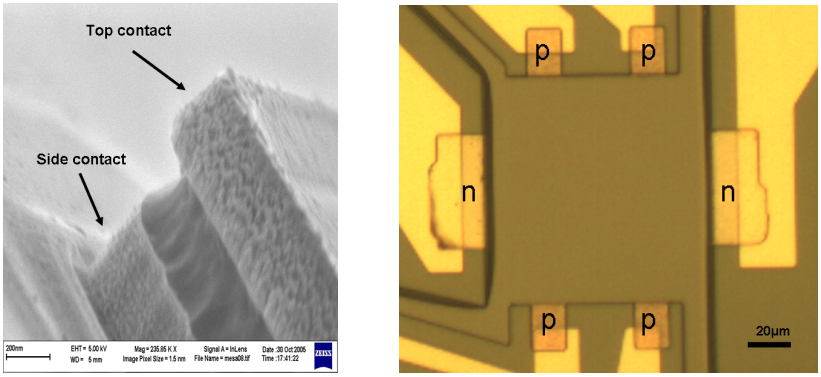


(a) (b)

Figure 2.3: (a) shows a SEM image of the mesa with top and side contacts. (b) shows microscope image of the side contacts geometry ($n$-type and $p$-type) and the mesa. Similar geometries exist also for only $n$-type contacts and only $p$-type contacts.

## 2.3 Experimental setup

The mesa was illuminated uniformly by a tunable Ti:Sapphire laser. Photoluminescence spectra (PL) was collected and analyzed, using a spectrometer. Since the QWs are asymmetric, it is possible to choose the excitation energy $E_L$ to be above or below the narrow well gap $E_{NW}$ (but always above the wide well gap $E_{WW}$). At $E_L < E_{NW}$ electrons and holes are excited in the wide well only ($E_{WW} < E_{NW}$). The electrons quickly tunnel into the narrow well (due to the applied electric field) and at steady state one gets nearly complete charge separation: the electrons reside in the narrow well while the holes are in the wide well. However, when $E_L > E_{NW}$ electrons and holes are created in both wells. Since the tunneling time of the holes is much longer than that of the electrons we get a population of holes trapped at the narrow well. Therefore, there is a mixture electrons and holes in the narrow well, and also holes in the wide well.

There are several advantages for this optical technique compared to the techniques mentioned in the introduction (see section 1.1.3). First, optical excitation generates equal number of electrons and holes ($n = p$). In the other techniques, it was difficult to maintain equal densities, issue that may influence the carriers interaction and cause screening (in case of inequality) [20]. Secondly, because the layers are undoped and the excited electrons tunnel into the narrow well, there is no need to apply a strong electric field. In addition, a very thin barrier can be used ($50\mathring{A}$).

A thin barrier does not prevent recombination entirely, so luminescence measurements can be made and provide insight into the system. Furthermore, there are two parameters we can use to tune the carriers density. Setting the electric field and thus the spatial separation of the electrons and the holes adjusts the excitons lifetime. In addition, by setting the excitation laser power a good control over the carriers density can be achieved.

The sample was immersed in superfluid helium, in a $^4$He cryostat, at (lattice) temperature of about $T = 1.5K$. A heater and PID control loop feedback technique enabled us to measure in higher temperatures as well (all measurements were done in lattice temperature of $T = 1.5K$, unless noted otherwise). The excitation energy was chosen to be in the region of 1540-1610 meV. Photoluminescence (PL) was collected from the mesa into a spectrometer.

The drag measurements were performed using the scheme described in Fig. 2.4. An AC current $I_{drive}$ of 10 nA at 131 Hz (using Keithley 6221 current source) was sent in the electrons (drive) layer, while a voltage $V_{drag}$ was measured across the holes (drag) layer, using a transformer (Eg&g, Princeton applied research, model 1900 low noise transformer), low noise voltage preamplifier (Stanford SR560) and lock-in amplifier (Stanford SR830). We verified that the measured drag voltage was linear in the driven current and independent of the AC current frequency for a large frequency range.

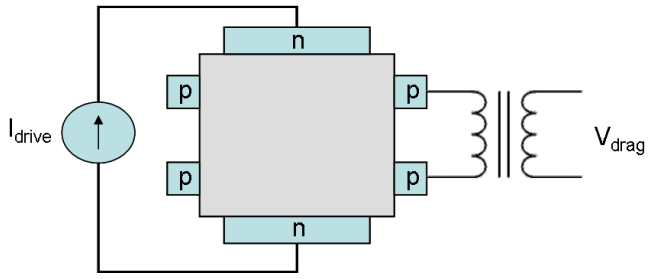


Figure 2.4: Measurement setup for the drag measurements. $I_{drive}$ was driven through the $n$-type contacts using a floating current source, while $V_{drag}$ was measured between the $p$-type contacts using low noise transformer, low noise voltage preamplifier and lock-in amplifier.

## 2.4 Sample characterization

### 2.4.1 Lifetime calculation

In an equilibrium, the carriers generation rate is equal to the recombination rate. For carriers density $n$ the recombination rate is given by $n/\tau$, where $\tau$ is the carriers lifetime. Therefore, in order to get the carriers density we have to calculate their lifetime.

#### Influence of the electric field

The perpendicular electric field strength determines the spatial separation of electrons and holes in the wells. When the applied electric field is raised, the wavefunctions of the electrons and the holes will be more confined to the edges of the wells, thus their overlap integral will be reduced. The recombination rate of excitons is proportional to the electron-hole overlap integral [34, 35], which can be written as:

$$\Sigma = \left| \int \chi_e(z_e)\chi_h(z_h)\delta(z_e - z_h)\, dz_e dz_h \right|^2 \tag{2.1}$$

where $\chi_e, \chi_h$ are the wavefunctions of an electron and a hole, respectively. Therefore, changing the strength of the electric field modifies the carriers lifetime, thus changing the steady state carriers density. This dependence of the lifetime on the applied electric field was demonstrated experimentally by Alexandrou *et al.* [35], who showed that the lifetime of indirect excitons is longer by three orders of magnitude in strong electric field compared to zero electric field state.

The electric field changes also the indirect excitons energy. In the absence of an electric field the optical transition with the lowest energy is the wide-well exciton recombination. By applying a perpendicular electric field $F$ the energy levels of the two wells are tuned such that the indirect exciton becomes the lowest-energy interband excitation, see Fig. 2.1a. The indirect exciton energy depends linearly on the electric field $F$ with a slope that is proportional to the separation distance between the two well centers $d$ [36]. It can be directly obtained from first order perturbation theory:

$$\Delta E_{IX}(F) = \langle\, \Psi(r_e, r_h) \,|\, eF(z_e - z_h) \,|\, \Psi(r_e, r_h) \,\rangle \approx eFd \tag{2.2}$$

The direct exciton experiences a small quadratic Stark shift, related to the product

of the induced dipole and the electric field $F$ [37].

Computing the carriers lifetime requires the evaluation of the electron and hole wavefunctions overlap integral in the CQWs, taking into account the effective electric field, see Eq. (2.1). A numerical calculation of the wavefunctions in the CQWs with an applied electric field, using *COMSOL Multiphysics*, results in the overlap integral, which is inversely proportional to the electron-hole pair lifetime $\tau$. The calculation consists of numerically solving the Schrödinger equation for an electron and a hole (with the appropriate effective masses and charge) for a potential of CQWs with an external electric field $F$. The lifetime is inversely proportional to the overlap integral of the ground state wavefunctions, for each value of the electric field $F$. In addition, the ground state energies are obtained.

Fig. 2.5a shows the calculated wavefunctions for several electric field strengths. For weak electric field both the electrons and the holes are in the same well. When the electric field is strong enough the electrons can tunnel into the other well, thus reducing their wavefunctions overlap integral.

Fig. 2.5b shows the lifetime as is calculated from the wavefunctions overlap integral, such that it is normalized by the zero-field lifetime (direct exciton in the wide well). Indeed, when the electric field is strong enough the lifetime increases by almost three orders of magnitude compared to the zero-field lifetime (1 ns compared to 1$\mu$s) due to the spatial separation. These calculations agree with previous experimental results [35, 38].

### 2.4.2 Photoluminescence measurements

In order to characterize the low-density properties of the system, the mesa was illuminated with very low power ($P < 1mW/cm^2$), and PL was measured as a function of the applied gate voltage. The measured spectra are presented in Fig. 2.6. One can clearly see the energies of the direct exciton in the wide well (X), the trion (T) and the indirect exciton (IX) which has a large redshift, as described by Eq. (2.2). These energies and the linear slope of the IX redshift are compared with the numerical calculation described above, thus enable us to match the applied gate voltage with the corresponding effective electric field. The numerical calculation agrees very well with the measurement (both direct exciton energy and IX slope).

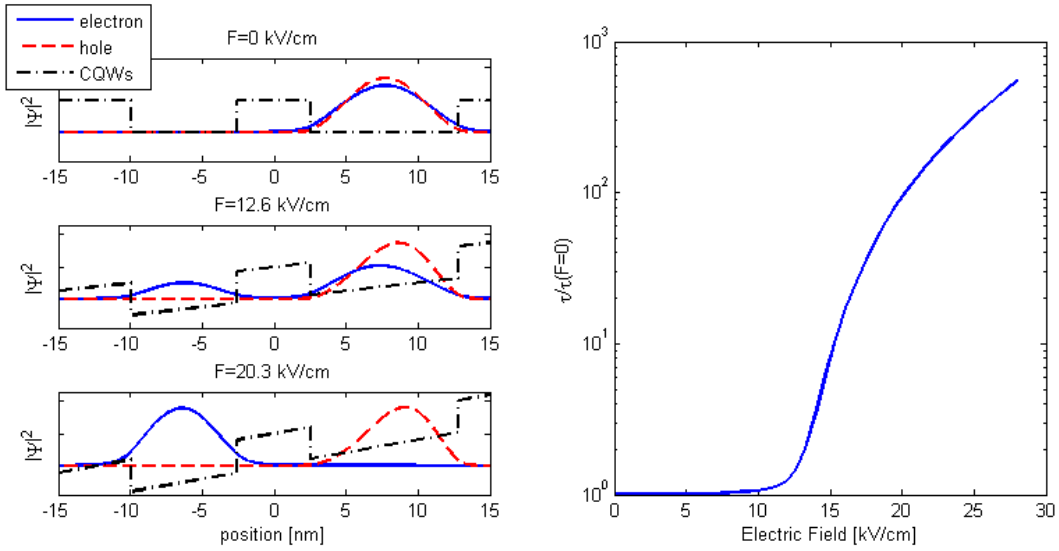


(a) (b)

Figure 2.5: (a) Calculated ground state wavefunctions of an electron and a hole in CQWs, with several electric field strengths. Notice the spatial separation of the electron and the hole into the different QWs. (b) Electron-hole lifetime as a function of the applied electric field, normalized by the zero-field lifetime (direct exciton in the wide well). Calculated from the overlap integral of the wavefunctions.

### Influence of the carriers density

The carriers density has a significant influence on the interactions, and consequently on the recombination energy. In an ideal, uncorrelated, electron-hole plasma, the separation of charges in the two wells creates a counter electric field, $F_c(n)$, which screens out the external electric field, and shifts the recombination energy to higher values (blueshift). The screening is proportional to the density of separated charges, like in a capacitor, and this blueshift can be directly calculated using Eq. (2.2) as:

$$\delta E(n) = (2\pi\varepsilon)^{-1} \int_0^\infty n \left( \frac{e^2}{r} - \frac{e^2}{\sqrt{r^2+d^2}} \right) 2\pi r dr = \frac{ne^2 d}{\varepsilon} \tag{2.3}$$

where $n$ is the density of the uncorrelated electron-hole plasma, $d$ is the separation between the centers of the two wells and $\varepsilon$ us the dielectric constant.

Therefore, as the density (illumination power) increases, the IX energy experiences a blueshift, as described by Eq. (2.3). For each value of the gate voltage, denote $E^0_{IX}$ as the IX energy at very low density (no blueshift). We can deter-

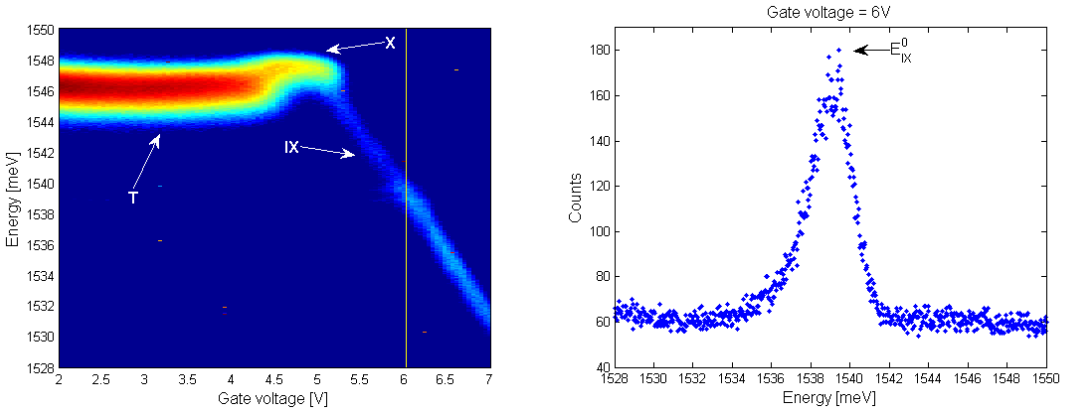


(a) (b)

Figure 2.6: Photoluminescence measurement as a function of the gate voltage. Excitation energy was tuned at 1590 meV with low illumination power density ($P < 1mW/cm^2$). The lattice temperature was $T = 1.57K$. (a) shows the spectra as a function of the applied gate voltage, and (b) shows the IX spectrum for gate voltage of 6V (yellow line in (a)). Notice the transition from trion (T) to exciton (X), and the large redshift of the indirect exciton (IX), according to Eq. (2.2).

mine $E^0_{IX}$ from the low-density measurement shown in Fig. 2.6. Fig. 2.6b shows a typical spectrum and $E^0_{IX}$ for gate voltage of 6V.

Note that at the excitonic regime Eq. (2.3) does not hold, since the energy shift is modified due to the correlations between excitons. Indeed, indirect excitons are arranged as parallel dipoles, pointing to the same direction and, thus, exercise a repulsive force on each other. In a simplified picture, each exciton creates a depletion region $\Delta(T)$ around itself, and the blueshift can be calculated as $\delta E_{int}(n) \approx (2\pi\varepsilon)^{-1} \int_{\Delta(T)}^{\infty} n \left( \frac{e^2}{r} - \frac{e^2}{\sqrt{r^2+d^2}} \right) 2\pi r dr$. A more rigorous theoretical description of these exciton-exciton interactions in CQWs was formulated by Schindler and Zimmermann [39, 40]. They showed a dramatic reduction of the interaction energy in low temperatures, which is manifested in the indirect excitons blueshift:

$$\delta E_{int}(n) = \frac{ne^2 d}{\varepsilon} f(T) \tag{2.4}$$

The factor $f(T)$ is small at cryogenic temperatures, $f(2K) = 0.08$, and its origin is the strong depletion around each exciton.

### Density and temperature calculation

Typical measurement of PL spectrum as a function of the illumination power is shown in Fig. 2.7a. When the illumination power is sufficiently low, a monotonic blueshift in IX energy as a function of the illumination power is seen. The carriers create a counter electric field $F_c(n)$, which screens out the external electric field (see section 2.4.2). When the illumination power is high enough, the counter electric field reduces the effective electric field, and the carriers lifetime becomes shorter. At this point, the IX energy reaches the X energy (due to the blueshift) and X are created. When the density is much larger, trions (T) are created.

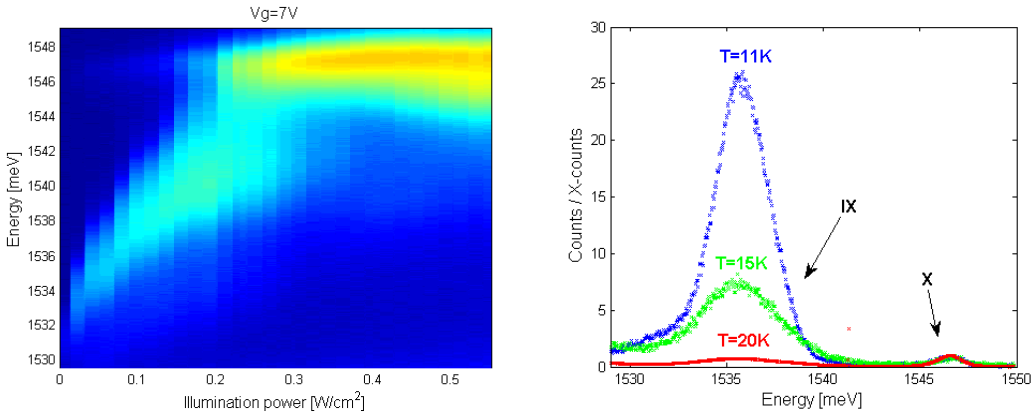


(a) (b)

Figure 2.7: (a) Typical PL spectra as a function of the illumination power, in gate voltage of 7V. The IX energy experiences large blueshift until it reaches the X energy. (b) PL spectrum for several temperatures. The temperatures were calculated according to the method described in section 2.4.2. Each spectrum is normalized relative to its X energy peak height. As the temperature is reduced the ratio of $P_{IX}/P_X$ becomes larger, according to Eq. (2.9).

Using simple thermodynamic equilibrium arguments for the X and IX populations, and the assumption of steady state in which the carriers generation rate $G$ is equal to the sum of the radiative recombination rates $P_X, P_{IX}$ we obtain

$$G = P_X + P_{IX} = \frac{n_X}{\tau_X} + \frac{n_{IX}}{\tau_{IX}} \quad (2.5)$$

$$n_X = n_{IX} \exp(-\Delta E/k_B T) \quad (2.6)$$

$$\Delta E = E_X - E_{IX} = E_X - E^0_{IX} - n_{IX} e^2 d/\varepsilon \quad (2.7)$$

where $_X$,$_{IX}$ represent direct and indirect electron-hole properties, respectively, $n$ is

density and $\Delta E$ is the direct-indirect recombination energy difference, according to Eq. (2.3).

Since the lifetime $\tau_{IX}$ is a function of the effective electric field $F - F_c(n)$, and thus a function of $G$, Eq. (2.5-2.7) should be solved self-consistently, using the numerically calculated lifetime.

Eq. (2.5-2.7) then give the following result:

$$G = \frac{n_{IX}}{\tau_X}\left(\frac{\tau_X}{\tau_{IX}} + \exp\left(-\frac{\Delta E}{k_B T}\right)\right) \tag{2.8}$$

Since the system is not completely in equilibrium with the lattice, especially when the illumination is high, the carriers temperature is not necessarily equal to the lattice temperature. The carriers temperature is determined by the ratio $P_X/P_{IX}$ of the PL intensities of X and IX, according to Eq. (2.9):

$$\frac{P_X}{P_{IX}} = \frac{\tau_{IX}}{\tau_X}\exp(-\Delta E/k_B T) \tag{2.9}$$

At low temperatures ($k_B T \ll \Delta E$) the IX recombination is much stronger than the X recombination ($P_X/P_{IX} \ll 1$), while at higher temperatures ($k_B T \gg \Delta E$) the IX recombination is much weaker than the X recombination ($P_X/P_{IX} \gg 1$). Fig. 2.7b shows several spectra in which the different ratios of the integrated intensity of X and IX recombinations represent different temperatures.

We use the PL measurements to solve Eq. (2.8-2.9) self-consistently, and hence determine the carriers density and temperature. The detailed method is described in Appendix C.

In order to check the validity of this method, it is possible to look at the density at which trions appear in the PL spectra. The transition from excitons to trions (X→T) is predicted to occur when the screening is strong enough [41], i.e. $q_s a_B \approx 2$, where $q_s$ is the screening wave-vector and $a_B = \frac{4\pi\varepsilon\hbar^2}{me^2}$ is the 3D excitonic Bohr radius. We performed PL measurements in several temperatures, similar to the measurement described in Fig. 2.7a. For each measurement we calculated the carriers density and temperature, and looked at the density at which trions appeared. Using the Thomas-Fermi approximation for the screening wave-vector, and the measured X→T density and temperature we got $1.6 < q_s a_B < 2.1$ for all the measurements, with an agreement with the theoretical prediction.

### 2.4.3 Transport measurements

In order to characterize the transport properties of the system we have measured the electrons conductance. The mesa of $n$-type contacts was illuminated uniformly and conductance was measured by driving AC current of 30nA (using current source) and measuring voltage in a four-probe configuration (both using $n$-type contacts) using low noise voltage preamplifier and lock-in amplifier. By tuning the current frequency we got a behavior of a parallel RC circuit (see inset to Fig. 2.8). The impedance of this simple RC circuit is given by $Z = \frac{R}{1+i\omega RC}$, so we were able to extract both the resistance $R$ and the capacitance $C$ from the frequency-dependant measurement, for each illumination power. By looking at the large $\omega$ regime of the out-of-phase component $Y \sim 1/\omega C$ we could extract $C$. The extraction of $R$ was made by calculating $|Z|\sqrt{1+\tan^2\theta}$ where $\theta$ is the measured phase.

Fig. 2.8 shows the measured impedance for several illumination powers. It fits very well to the RC circuit impedance. Therefore, for the drag measurement the relevant drag resistance should be calculated as:

$$R_D = |V_D/I| = |V_D/I_0|\sqrt{1+\tan^2\theta} \tag{2.10}$$

where $I$ is the current that flows through the resistor in the drive layer, $I_0$ is the current generated by the current source, $V_D$ is the measured drag voltage amplitude and $\theta$ is the measured phase.

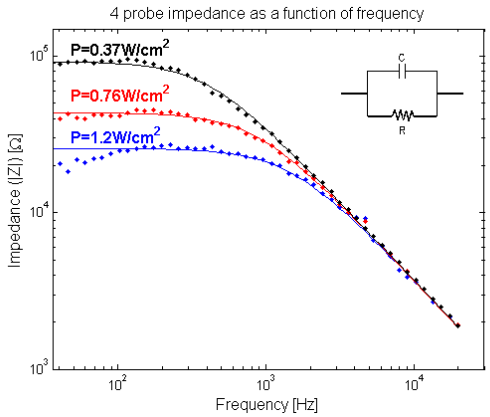


Figure 2.8: Impedance of electrons (four-probe configuration) as function of the AC current frequency $\omega/2\pi$. In the low $\omega$ regime $|Z| \sim R$ and in the high $\omega$ regime $|Z| \sim 1/\omega C$. The solid points are the measurement data and the solid lines are the fit to an RC circuit impedance. Inset shows the RC circuit that the transport measurements correspond to.

Notice that when the measured signal is in-phase with the driven current, no correction should be done. However, in a regime in which the measured signal has a significant out-of-phase component we can use Eq. (2.10) in order to get the drag resistivity in this regime as well. We verified that this correction indeed gives the same result for measurements in different frequencies (see section 3.1.4).

Repeating the method for several illumination powers gave a constant capacitance of $C = 4.3 \pm 2\text{nF}$ and conductance that increases with the illumination power.

# Chapter 3

# Results

## 3.1 Coulomb drag characterization

### 3.1.1 Linear response regime

The measurements should be done in the linear response regime, in which the drag voltage is linear in the driven current. In order to verify it we measured the drag voltage as a function of the current, as shown in Fig. 3.1. We can see that for low enough currents the voltage signal is linear in the driven current, and drag resistivity can be easily defined as in Eq. (1.3). Therefore, we worked with a typical current of $10 - 20$nA, which was clearly in the linear response regime.

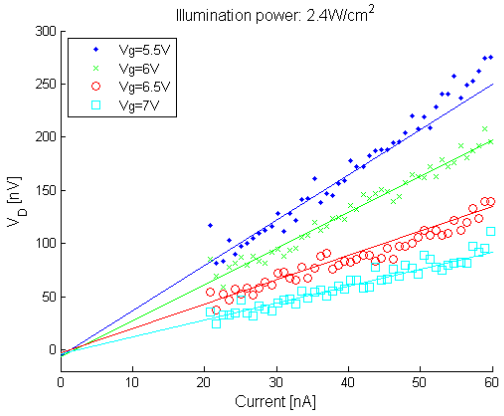


Figure 3.1: Drag voltage $V_D$ as a function of the driven current, for several gate voltages $V_g$ and illumination power $2.4W/cm^2$.

### 3.1.2 Light absorption in quantum wells

It is crucial to confirm that the measured results were indeed caused by the light absorption (carriers generation) in the QWs. The drag resistivity was measured as a function of the excitation energy $E_L$ (laser wavelength) and with constant illumination power, as shown in Fig. 3.2a. It exhibits several deeps that are related to absorption lines in the QWs.

To establish this correspondence, Fig. 3.2b presents the absorption spectrum of our system obtained by photoconductivity measurements as a function of the excitation energy $E_L$. The four observed peaks (deeps) in the photoconductivity (drag resistivity) correspond to the absorption lines of the heavy-hole (hh) and light-hole (lh) excitons in the wide (WW) and narrow (NW) wells - $E^{hh}_{WW}$,$E^{lh}_{WW}$,$E^{hh}_{NW}$ and $E^{lh}_{NW}$ respectively (see inset to Fig. 3.2b).

This correspondence establishes that the measured drag voltage is absorption-dependent and is related to the carriers' density in the QWs. Higher absorption is manifested in higher conductivity and lower drag resistivity. When the excitation energy is tuned below the energy band gap, the absorption in the QWs is negligible, and indeed the photoconductivity is very low and the drag resistivity is high.

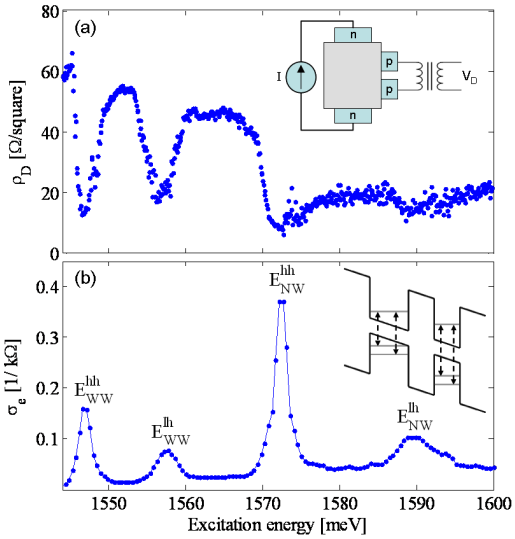


Figure 3.2: (a) Drag resistivity as a function of the laser excitation energy, for illumination power of $0.4W/cm^2$ and gate voltage of 6V. (b) Photoconductivity, measured in a four-probe configuration, as a function of the laser excitation energy. The conductivity was measured at frequency of 13 Hz, illumination power of $4W/cm^2$ and gate voltage of 6V. It reflects the light absorption spectrum. The inset shows the corresponding excitonic absorption lines in the QWs.

### 3.1.3 Illumination power dependence

The dependence of the drag resistivity on the illumination power reveals some important issues. Fig. 3.3a shows such typical measurement. It is very clear that the drag resistivity decays by almost two orders of magnitude as the illumination power increases. The decay is expected due to stronger screening when the density is high (see section 1.1.2).

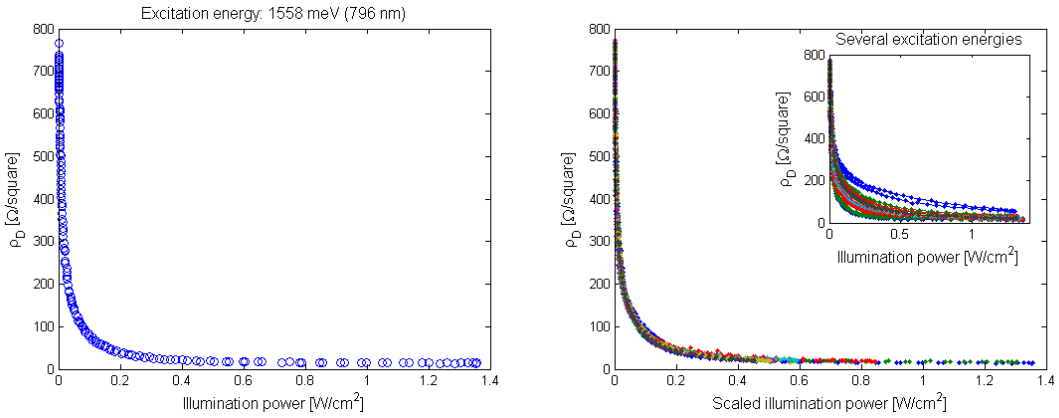


(a) (b)

Figure 3.3: (a) Drag resistivity as a function of the illumination power for excitation energy of 1558 meV, at gate voltage of 6V. The drag resistivity decays by almost two orders of magnitude as the illumination power increases. (b) Drag resistivity as a function of the scaled illumination power for several excitation energies in the range 1552-1565 meV, at gate voltage of 6V. Inset shows the measured (unscaled) data. It can be seen the by scaling the power axis all these curves collapse into a single curve.

In order to further verify that indeed the drag resistivity depends on the light absorption in the QWs, we measured the drag resistivity as a function of the illumination power for several excitation energies in the range 1552-1565 meV. We scaled the illumination power of each excitation energy by the corresponding absorption coefficient. The measurements and the scaling are shown in Fig. 3.3b. It can be seen that indeed by scaling the illumination power the different measurements collapse together, as expected if the different excitation energies express different absorption coefficients.

### 3.1.4 Current frequency dependence

As already mentioned in section 2.4.3, due to the RC circuit behavior of the system, we have to make adjustments to the drag resistivity measurements in order to consider the capacitive effect on the measured phase. Therefore, as described by Eq. (2.10), the drag resistivity is calculated using both the measured amplitude and the measured phase. Fig. 3.4 shows results of drag measurements in different AC frequencies as a function of the illumination power. In the inset we can see the measured drag resistivity amplitude $V_D/I_0$ where $V_D$ is the measured drag voltage and $I_0$ is the driven current (by the current source). It is clear that the results of these measurements are different due to the different frequencies, despite we do not expect such frequency dependence effect of the drag resistance.

When we use the method described by Eq. (2.10), which takes into account the RC circuit effect, we see that these different drag resistivity measurements agree, as can be seen in the main plot in Fig. 3.4.

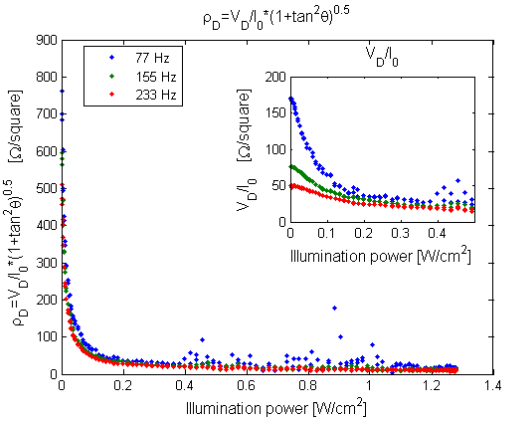


Figure 3.4: Drag resistivity as a function of illumination power, for several frequencies of the AC current and gate voltage of 7V. The inset shows the drag resistivity amplitude $V_D/I_0$, while the main plot shows the method described by Eq. (2.10) which takes into account the RC circuit effect. Clearly the latter method describes the system better.

## 3.2 Coulomb drag measurements

Measurement of the drag resistivity as a function of the illumination power was made at gate voltage of 7V, excitation energy of 1590 meV and lattice temperature of 1.5 K. Simultaneously with the drag resistivity measurement PL had been collected, enabled the extraction of the carriers density and temperature using the method described in section 2.4.2. The calculated carriers temperature was 5 K. Fig. 3.5a shows the dependence of the drag resistivity on the illumination power, and Fig. 3.5b shows the same measurement as a function of the carriers density, as was calculated using the described method. The drag resistivity decays by two orders of magnitude as the density increases. The decay is expected to occur due to screening effects (see section 1.1.2).

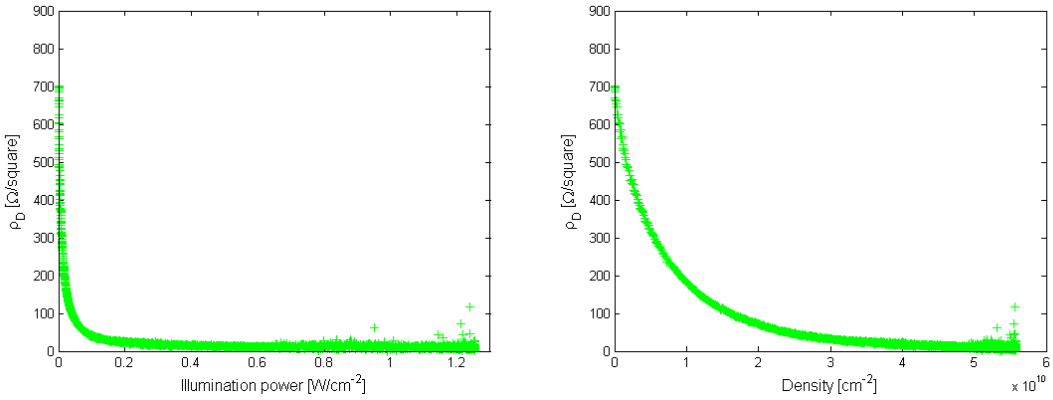


(a) (b)

Figure 3.5: Drag resistivity as a function of (a) the illumination power and (b) the carriers density. The measurement was done at gate voltage of 7V, excitation energy of 1590 meV and lattice temperature of 1.5 K. The calculated carriers temperature was 5 K.

Additional measurements of the drag resistivity as a function of the illumination power were made in several temperatures (using a heater and PID controller) and excitation energies (1558, 1565, 1590 meV). Fig. 3.6 shows the dependence of the drag resistivity on the carriers density and temperature. A decay of the drag resistivity with respect to the density is seen. The decay rate decreases when the temperature becomes higher, at least at low densities. Another temperature-related phenomenon is an increase in the drag resistivity when the temperature increases, as predicted due to the joint phase space for scattering processes, see

section 1.1.2.

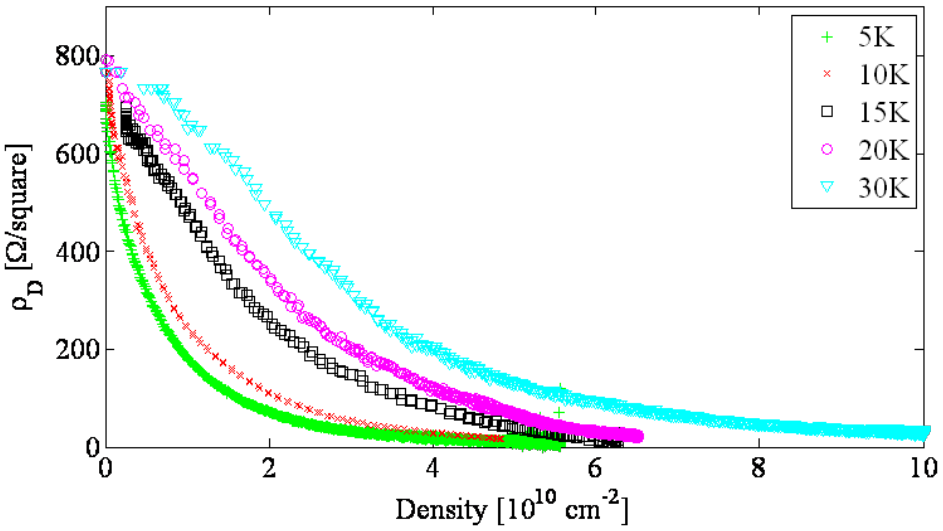


Figure 3.6: Drag resistivity as a function of the carriers density in several temperatures, at gate voltage of 7V. The carriers density and temperatures were extracted using the low illumination power PL spectra, as described in section 2.4.2. Similar results are obtained for more temperatures, here presented only a few for clarity.

### 3.2.1 Coulomb drag - different regimes

The dependence of the drag resistivity on the density and temperature distinguishes between two regimes. It is convenient to examine it in logarithmic scales, as shown in Fig. 3.7 for some typical measurements. Two different regimes are seen as a function of density.

At low densities, as seen in Fig. 3.7a, the drag resistivity decays exponentially as a function of concentration. The decay rate $\gamma$ is temperature-dependent - as the temperature increases, $\gamma$ becomes lower. In fact, $\gamma^{-1}$ is approximately linear in temperature, i.e. $\gamma^{-1} = \alpha T + \beta$, as can be seen in Fig. 3.8. We find that at low densities, the drag resistivity can be written as:

$$\rho_D = \rho_0 T \exp\left(-\frac{n}{\alpha T + \beta}\right) \tag{3.1}$$

where $\rho_0 \approx 50\Omega \cdot \mathrm{K}^{-1}$ and $\beta/\alpha \approx 20\mathrm{K}$.

At high densities, a deviation from the exponential decay is observed. Fig. 3.7b

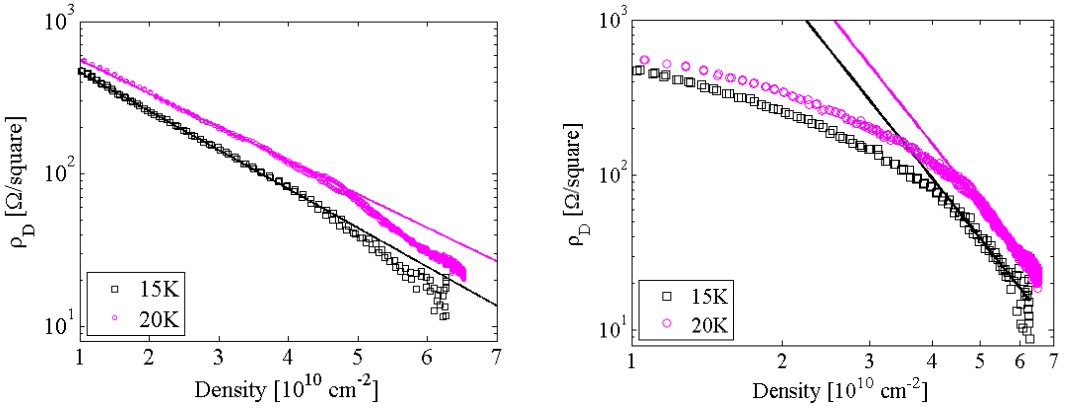


Figure 3.7: Drag resistivity as a function of the carriers density, in several temperatures. In the low-density regime, (a) shows an exponential decay of the drag resistivity with respect to the density. In the high-density regime, (b) shows a power-law decay of the drag resistivity (indeed (a) shows deviation from exponential curve at high densities). Similar results are obtained for more temperatures as well. Only a few are presented here, for clarity.

shows the same drag resistivity measurements as in Fig. 3.7a, in a log-log scale. Indeed, when the density reaches $4-5\times10^{10}cm^{-2}$ the curves change, and linear slope (in the log-log scale) is seen. The linear slope for the high-density regime indicates a power-law rather than an exponential decay, $\rho_D(n,T)\sim n^{-b}$.

Furthermore, the drag resistivity dependence on the density and temperature becomes separable: $\rho_D(n,T)=\rho_n(n)\cdot\rho_T(T)$. In order to show it, we normalize the drag resistivity with respect to a constant density or a constant temperature. This can be seen in Fig. 3.9a, which presents the normalized drag resistivity $\frac{\rho_D(n,T)}{\rho_D(n_0,T)}$, for several temperatures, where $n_0=4.5\times10^{10}\mathrm{cm}^{-2}$. For densities higher than $n_0$ the different curves collapse to a single curve, which is a manifestation of the separability. This single curve shows the density dependence of the drag resistivity in this regime. The inset of Fig. 3.9a presents the temperature-averaged curve of this collapse (the error-bars represent the standard deviation). It fits very well to a power-law relation, in which the power-law exponent $b$ is found to be in the range of $2.6\pm0.1$: $\rho_n(n)\sim n^{-2.6}$.

In order to determine the temperature dependence $\rho_T(T)$, we normalized the drag resistivity by its value at $T_0=30$K: $\frac{\rho_D(n,T)}{\rho_D(n,T_0)}$. The result is shown in Fig. 3.9b, with the appropriate error-bars (standard deviation for the density). It is seen that

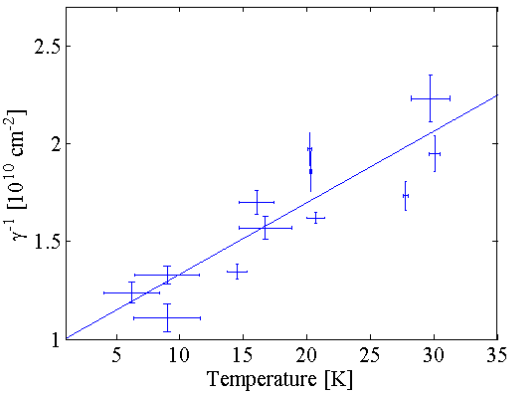


Figure 3.8: The inverse decay rate $\gamma^{-1}$ of the drag resistivity at low densities is plotted as a function of temperature (error-bars). The solid line is a linear fit for the data, such that approximately $\gamma^{-1} = \alpha T + \beta$.

the data fits well to a $T^2$ curve (notice that the solid line is not a fit to the data but a $(T/T_0)^2$ curve). Hence, we conclude that at high densities the drag resistivity has the following dependence:

$$\rho_D(n, T) \sim \frac{T^2}{n^{2.6}} \tag{3.2}$$

These results are very significant. The drag resistivity in the high-density regime exhibits a quadratic temperature dependence and a power-law decay with respect to the density. This behavior agrees with the theoretical prediction for Coulomb drag within the Fermi-liquid theory [6] (see also Fig. 1.2 and Appendix A), and with previous experimental observations [5, 15, 22, 21]. However, in the low-density regime an exponential decay of the drag resistivity is observed for the first time. A transition between an exponential and a power-law decay is seen.

### 3.2.2 A percolation-like transition

#### The origin of the exponential decay

We purpose a possible model to describe the exponential decay of the drag resistivity at low densities (with a collaboration with B. Laikhtman [42]). A percolation model for 2D electron gas [43, 44, 45] suggests that a disorder potential created by impurities or surface roughness forms density puddles connected by saddle points (since the potential fluctuations due to disorder cannot be screened). At low con-

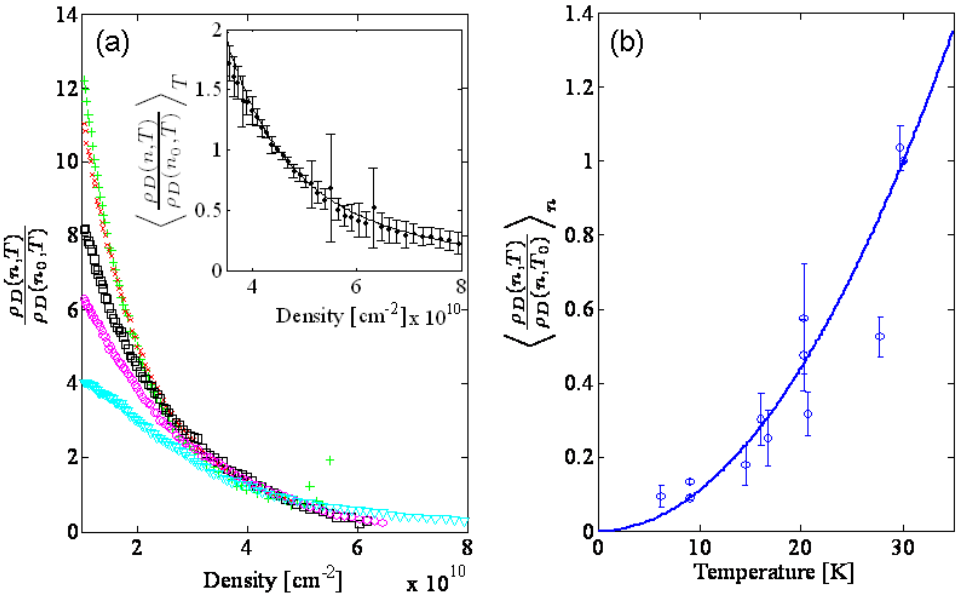


Figure 3.9: (a) The drag resistivity for several temperatures, normalized by its value at $n_0 = 4.5 \times 10^{10}\text{cm}^{-2}$. At high densities the different curves collapse to a single curve, which is a manifestation of the separability. The inset shows the temperature-averaged curve of this collapse (the error-bars represent the standard deviation). The solid line is a fit for a power-law: $\rho_n(n) \sim n^{-2.6}$. (b) The drag resistivity, normalized by its value at $T_0 = 30\text{K}$. The solid line is a $(T/T_0)^2$ curve.

centration the Fermi level is below the critical saddle point (or a few of them) and the transport takes place due to activation or tunneling across the saddle points. At high concentration the Fermi level is above the critical saddle point and the system is metallic. Indeed, the drag resistivity at high densities agrees with the predicted and observed behavior of Fermi-liquid.

The experimental results are well described by activation temperature dependence with activation energy $E_c - E_i$, where $E_c$ is the energy level of the critical saddle point and $E_i$ is a highest electron level. The highest electron level is the Fermi energy plus the Coulomb interaction energy. The same Coulomb energy defines the blueshift of the luminescence line. Since the blueshift is proportional to the density (for density which is not very low, see Eq. (2.3)), we expect a resistivity dependence of the form

$$\rho \sim \exp\left[-\frac{\delta E(n)}{k_B T}\right] \qquad (3.3)$$
$$\delta E(n) = \frac{e^2 d}{\varepsilon} n = \alpha^{-1} n$$

Taking $d$ as the separation between the quantum wells we get $\alpha$ with good agreement with the experimental value, see Fig. 3.8 and Eq. (3.1). The fact that we have an effective temperature term $\beta/\alpha$ (Eq. (3.1)) can be explained by broadening effects due to disorder and mainly interactions (which may be manifested as a different, wider momentum distribution function).

### Transition in single-layer resistance

A transition between a disordered state (puddles) and a metallic behavior should affect also the single-layer properties, such as single-layer resistance. Therefore, and in order to better understand the observed transition, we measured simultaneously the single-layer (electrons) resistance (four-probe configuration) and the PL spectrum. The resistance measurement is shown in Fig. 3.10 (gate voltage of 7V, carrier temperature of 15K), and exhibits an exponential behavior as well. When the density reaches a critical value of $n_c \sim 5.5 \times 10^{10}\,\mathrm{cm}^{-2}$, a significance deviation from the exponential dependence occurs - the resistance approaches the quantum resistance $h/e^2$ and experiences a sudden drop.

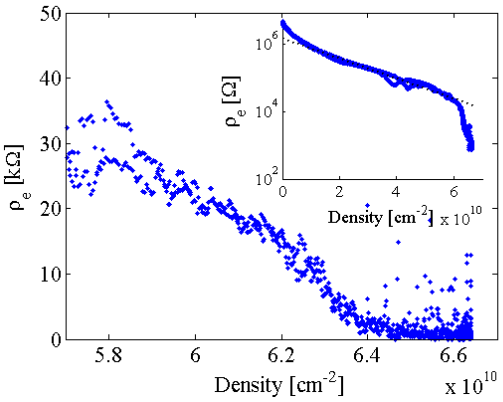


Figure 3.10: Electrons resistance measurement (four-probe configuration) as a function of the density. The main plot focuses on the high-density regime, where a drop in resistance occurs at about $h/e^2$. Inset shows the same measurement, semi-logarithmically scaled. An exponential decay of the resistance is observed, similar to the drag resistivity decay. The gate voltage is 7V and the carriers temperature is 15K.

Simultaneously, the photoluminescence spectra were measured. Fig. 3.11 presents photoluminescence spectra for several densities. Near the critical density $n_c$, trions appear and the spectrum exhibits an exciton-trion transition $\left(X^{hh}_{WW} \to T\right)$.

The abrupt drop in the resistance near the quantum resistance suggests that the observed transition in the drag resistivity is caused by a percolation-like transition in the system. The appearance of trions in the photoluminescence spectra at about the same density is consistent with this description, since it has been observed near a metal-insulator transition in two-dimensional electron gas [46].

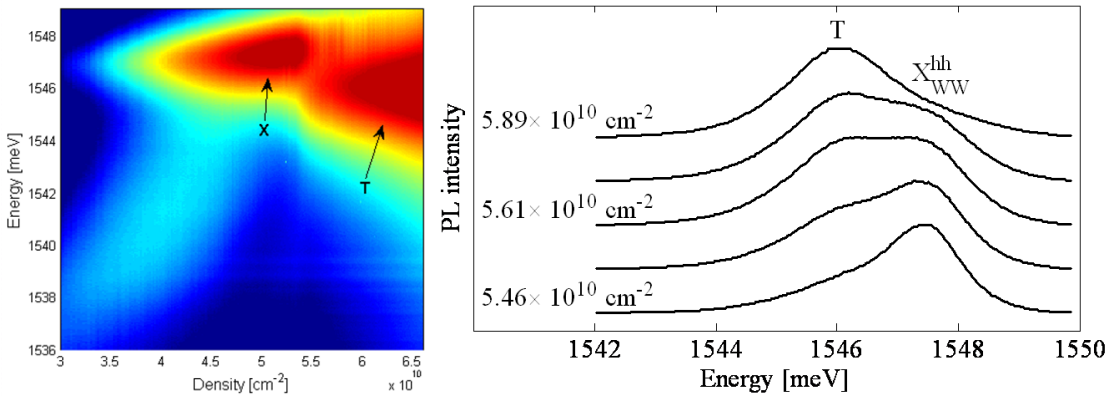


(a) (b)

Figure 3.11: (a) Photoluminescence spectra, measured simultaneously with the resistance shown in Fig. 3.10, as a function of the density. X, T represent excitons and trions, respectively. The colorbar is the PL intensity (a.u.), logarithmically. (b) shows several of these spectra, near the exciton-trion transition, with specified densities.

Both the drag resistivity, the single-layer resistance and the PL spectra are consistent with a percolation transition. In the high-density regime, the conductance is high (metallic behavior) and the drag resistivity shows the well-established dependence of a power-law with respect to the density and quadratic in temperature. In addition, the screening is strong enough so trions appear in the PL spectrum. At low densities, the resistance jumps to values of about the quantum resistance $h/e^2$ and the drag resistivity decays exponentially with respect to the density.

As discussed, such exponential decay may result from disorder effects [47, 48, 45]. Indeed, the carriers in the investigated bilayer may experience a disorder potential due to monolayer width fluctuations. Since the confinement energy in a quantum well depends on the well width $L$ as $E \propto 1/L^2$, fluctuations in the well width affect the energy as $\frac{dE}{E} = -2\frac{dL}{L}$. Thus, the disorder potential is significantly affected by fluctuations of well width when the quantum well is narrow. For wells of $70\mathring{A}$ and $100\mathring{A}$ and typical density of $5 \times 10^{10} cm^{-2}$ the fluctuations are in the

same order as the Fermi energy, an issue which may affect the scattering processes and hence the drag and single-layer resistivity.

### Appearance of noise

Another phenomenon, which occurs in the high-density regime, is the appearance of noise. As we saw, the drag resistivity decays as the density increases. When the density reaches some value, the measured signal becomes much noisier than it was below that density (noise both in amplitude and in phase). This sudden appearance of noise could already be seen in Fig. 3.7a and Fig. 3.7b. It is seen even better in Fig. 3.12, and is reproducible.

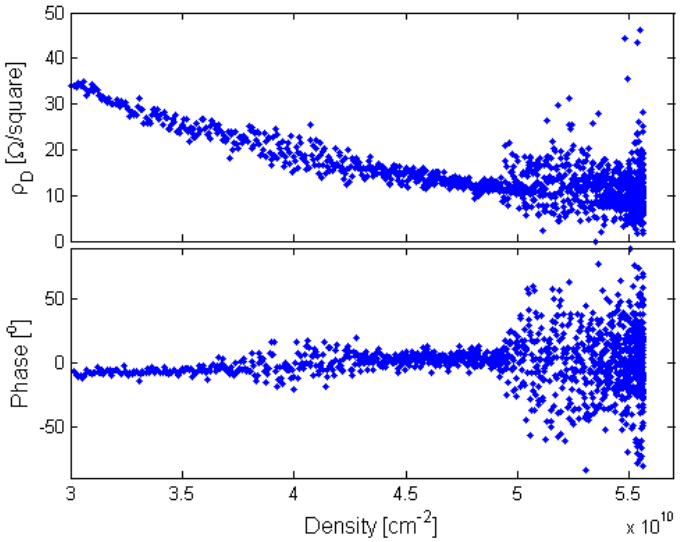


Figure 3.12: Drag resistivity as a function of the density. The upper plot shows the drag resistivity while the lower plot shows the measured phase. Noise appears for densities higher than about $5 \times 10^{10} cm^{-2}$, both in the measured amplitude and in the phase. The excitation energy is 1590 meV and the gate voltage is 7V.

The source of this noise is still unknown, and also the dependence of the point it appears on the temperature, gate voltage and excitation energy (is it related to excitation in both wells rather than excitation only in one well [49]).

# Chapter 4

# Summary

In this work we have studied Coulomb drag in an electron-hole bilayer system. We introduced a new technique, in which the bilayer system was obtained using optically generated electrons and holes, which were separated between two coupled quantum wells by applying an electric field. In addition, a reliable method for fabricating ohmic contacts with the photo-excited carriers (either $n$-type or $p$-type) was presented. This technique enables the creation of an equal density electron-hole bilayer system ($n = p$), with much narrower barrier compared to previous studies, and without applying high voltages. It allows us to study the Coulomb drag at low densities, thus relatively large $r_s = \frac{E_{e-e}}{E_F} \approx a_B^{-1}(\pi n)^{-1/2}$ ($r_s$ reaches 6 at low densities and 1.6 at high densities).

The combination of transport and photoluminescence measurements is presented as a method for studying the carriers states in the system, and in particular extracting the carriers density and temperature. This is needed since the photo-excited carriers temperature may be different than the lattice temperature. In addition, Hall measurement for determining the density did not succeed, probably because of leakage currents and direct illumination on the ohmic contacts.

The dependence of the drag resistivity on the density and temperature reveals some notable features. In the high-density regime the drag resistivity decays as a power-law with respect to the density, and is quadratic in temperature. Both features were predicted theoretically [6] (see also Appendix A) and observed experimentally [5, 15, 22, 21] in bilayer drag studies, and are a signature of a drag measurements for Fermi-liquids.

We focus on the low-density regime - a regime which have not been studied

so far. We present the first observation of an exponential decay of the drag resistivity with respect to the density in the low-density regime, and suggest that the transition between the exponential and the power-law decay is a manifestation of a percolation transition. The percolation is seen very clearly in a single-layer resistance measurement as the resistance drops abruptly when it reaches $h/e^2$. In addition, trions appear in the photoluminescence spectrum. These three transitions - of the drag resistivity, the single layer resistance and the appearance of trions - occur at about the same density and are consistent with a percolation transition.

Studies predict an exponential dependence of the single-layer resistivity on the temperature and density, in the presence of disorder [47, 45] and near metal-insulator transition [50]. This may indicate a possible similar behavior for the drag resistivity as well [48].

Another phenomenon, which occurs in the high-density regime, is the somewhat sudden appearance of noise in the measured drag signal. This is still not understood and further research is required. Studying the possible relation between the appearance of noise and the percolation transition can contribute to the understanding of the electron-hole interactions and correlations in the bilayer system. The technique we presented allows measurements in a variety of systems and parameters - temperatures, densities, different wells. Further research may study the electron-hole bilayer system with less disorder (wider quantum wells) and in lower temperatures. These regimes might lead to exotic ground states and condensates which can be revealed by drag and counterflow transport measurements [25].

# Appendix A

# Theory of drag resistivity

As explained in section 1.1.2, the drag resistivity can be calculated within the Fermi-liquid theory. There are different regions of the density and temperature in which the drag resistivity dependence on these parameters is different. The results below are following Laikhtman [12].

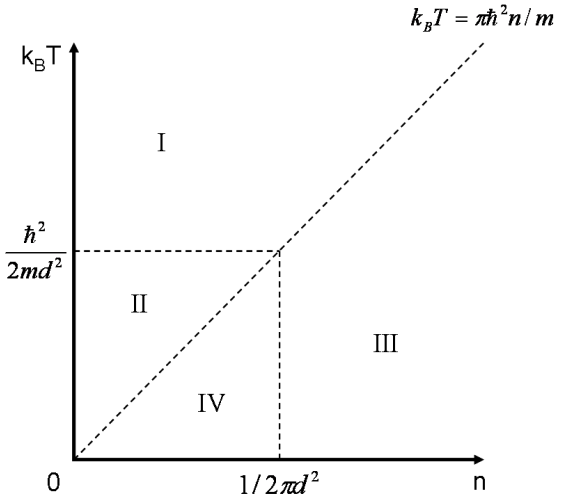


Figure A.1: Regions of the density and temperature where the drag resistivity dependence on these parameters is different.

It is convenient to sort the results according to degeneracy of the gas and momentum transfer, see Fig. A.1.

I. Non-degenerate gases ($k_BT > k_BT_F = \pi\hbar^2 n/m$) and wide barrier ($k_T d >$

$1 \Leftrightarrow k_B T > \hbar^2/2md^2$).

$$\rho_D = -\frac{\pi^{3/2} e_1 e_2 \left(m_1 m_2\right)^{1/2}}{\sqrt{2}\kappa^2 \left(m_1 + m_2\right)^{1/2} \left(k_B T\right)^{3/2} d} \tag{A.1}$$

II. Non-degenerate gases ($k_B T > k_B T_F = \pi\hbar^2 n/m$) and narrow barrier ($k_T d < 1 \Leftrightarrow k_B T < \hbar^2/2md^2$).

$$\rho_D = -\frac{4\pi^2 e_1 e_2 \left(m_1 m_2\right)}{\kappa^2 \hbar \left(m_1 + m_2\right) k_B T} \tag{A.2}$$

III. Degenerate gases ($k_B T < k_B T_F = \pi\hbar^2 n/m$) and wide barrier ($k_F d > 1 \Leftrightarrow n > 1/2\pi d^2$).

$$\rho_D = -\frac{\zeta(3) e_1 e_2 \left(m_1 m_2\right)^2 \left(k_B T\right)^2}{8\pi\kappa^2 \hbar^7 \left(n_1 n_2\right)^{3/2} \left(q_{s1} q_{s2}\right)^2 d^4} = -\frac{\pi^2 \zeta(3) \hbar \left(k_B T\right)^2}{16 e_1 e_2 \epsilon_{F1} \epsilon_{F2} \left(k_{F1} k_{F2} d^2\right) \left(q_{s1} q_{s2} d^2\right)} \tag{A.3}$$

IV. Degenerate gases ($k_B T < k_B T_F = \pi\hbar^2 n/m$) and narrow barrier ($k_F d < 1 \Leftrightarrow n < 1/2\pi d^2$).

$$\rho_D = -\frac{4 e_1 e_2 \left(m_1 m_2\right)^2 \left(k_B T\right)^2}{3\kappa^2 \hbar^7 Q_s^2 n_1 n_2} \ln \frac{k_{F1} + k_{F2}}{\left|k_{F1} - k_{F2}\right| + k_T^2/k_F} \tag{A.4}$$

Here $1, 2$ denote the two layers, $e, m, n$ are the particles charge, effective mass and density, respectively, $d$ is the layers separation, $T$ is the temperature, $\kappa$ is the dielectric constant, $\zeta$ is the Riemann zeta function, $\epsilon_F$ and $k_F$ are the Fermi energy and wave-vector, respectively, $k_T$ is the thermal wave-vector, $q_s$ is the screening wave-vector [11] and $Q_s = q_{s1} + q_{s2} + 2q_{s1}q_{s2}d$.

# Appendix B

# Sample preparation process

The usual procedure for making ohmic contacts to 2DEG/2DHG (depositing a metallic layer on the sample surface and annealing it) has proven to be problematic for intrinsic QWs, in which the carriers are photo-created. The photo-excited carriers do not form a good contact with the annealed region, and a non-linear $I$-$V$ curve is observed [29]. In order to solve the problem a technique in which the contacts are made to the *sides* of the QWs [30] has been developed [31].

First, top and back gate ohmic contacts to the $n^+$ layers were established by wet etching a mesa and evaporation of Ni 300$\mathring{A}$/Au 500$\mathring{A}$/Ge 500$\mathring{A}$/Au 500$\mathring{A}$ (no annealing), in the usual procedure.

Then, ohmic contacts to the QWs are established. In order to make these contacts self aligned and to the sides of the QWs the following procedure is used. A mesa is defined by anisotropic $SiCl_4$ plasma etching (dry etching) up to a depth of 2000$\mathring{A}$ above the QWs. The structure is then wet etched up to the depth of 1000$\mathring{A}$ below the QWs. Without removing the photo-resist a layer of $SiO_2$ is deposited (40 sec). This layer deposition protects the photo-resist and establishes the self-alignment of the QWs contacts. Then, a layer of image reversal photo-resist is patterned to define regions where the contacts will be deposited. These regions are both to the side of the mesa and on top of it. The $SiO_2$ is then removed only from the exposed regions (where the image reversal photo-resist was removed) using buffered oxide etch (buffered HF), and the contacts are established by evaporating either Ni 175$\mathring{A}$/Au 355$\mathring{A}$/Ge 315$\mathring{A}$/Au 355$\mathring{A}$ for $n$-type contacts or Ni 50$\mathring{A}$/Au 300$\mathring{A}$/Zn 500$\mathring{A}$/Au 1000$\mathring{A}$ for $p$-type contacts. The evaporation is executed on a rotating tilted stage. The photo-resists (image reversal and positive)

and $SiO_2$ are then removed using acetone, buffered HF and plasma (150 W, 5 mins). After the removal the evaporated contacts are located only to the sides of the QWs (sides of the mesa) since the evaporated metal on top of the mesa was removed due to the $SiO_2$ removal. Therefore, the contacts are self-aligned. This process is repeated twice - once for establishing the $n$-type contacts and once for establishing the $p$-type contacts. Then, the contacts are annealed at $370^o$C for 2 mins and $440^o$C for 50 sec. The result is a mesa with ohmic contacts to the sides of the QWs which can be either $n$-type or $p$-type, as seen in Fig. 2.2 and Fig. 2.3.

# Appendix C

# Density and temperature calculation

We can use PL measurement as a function of the illumination power (typical measurement is shown in Fig. 2.7a) to solve Eq. (2.9-2.8) self-consistently, and to extract the carriers density and temperature. The lifetime used in this calculation is the numerically calculated lifetime (see section 2.4.1).

To account for the density-dependent counter electric field (see section 2.4.2) one has to use $\tau_{IX} = \tau(F - F_c(n)) = \tau(F - n_{IX}e/\varepsilon)$ and $\tau_X \equiv \tau_0 = \tau(F = 0)$ where $\tau$ is the numerically calculated lifetime. Eq. (2.9-2.8) then give:

$$\frac{P_X}{P_{IX}} = \frac{\tau(F - F_c(n))}{\tau_0} \exp(-\Delta E/k_B T) \tag{C.1}$$

$$G = \frac{n_{IX}}{\tau_0} \left( \frac{\tau_0}{\tau(F - F_c(n))} + \exp\left( -\frac{\Delta E}{k_B T} \right) \right) \tag{C.2}$$

First, we use $E^0_{IX}$ (see section 2.4.2) and the energy dependence of the IX in order to get the IX blueshift and to compute the carriers density. Large blueshift, such as 4 meV or higher, results from the blueshift mechanism of free electron-hole recombinations as described by Eq. (2.3) (otherwise, adding the correlation factor $f(T)$ of Eq. (2.4) demands much higher densities, which is inconsistent with the excitonic regime this factor describes). Therefore, we may use Eq. (2.3) in order to get the carriers density in this large blueshift regime.

This density allows us, using Eq. (C.2), to calibrate $P$ for the entire measurement (including the absorption coefficient), and so, using the same equation, to extract $n_{IX}$ for the entire measurement. Note that $\Delta E$ depends on $n_{IX}$ in this

calculation.

Self-consistently, we may use a single spectrum in which both X and IX are visible in order to extract the carriers temperature. From the spectrum we get $\Delta E = E_X - E_{IX}$ and $P_X$,$P_{IX}$ which are the integrated intensities of the direct and indirect recombinations. Using Eq. (C.1) we can extract the carriers temperature. Fig. 2.7b shows several spectra in which the different ratio of the integrated intensity of X and IX recombinations represents different temperatures. As expected, at lower temperatures the IX recombination is much stronger than the X recombination.

Therefore, we have a technique in which by measuring PL at the low power regime we may extract both the carriers density and the temperature for the entire measurement (also for the high power regime). These optical measurements can be done simultaneously with transport measurements, allowing us to study the sample behavior in various ways.

# Bibliography


[1] J. P. Eisenstein and A. H. MacDonald, "Bose-Einstein condensation of excitons in bilayer electron systems.," *Nature*, vol. 432, pp. 691–4, Dec. 2004.

[2] J.-J. Su and A. H. MacDonald, "How to make a bilayer exciton condensate flow," *Nature Physics*, vol. 4, pp. 799–802, Aug. 2008.

[3] M. B. Pogrebinskii, "Mutual Drag of Carriers in a Semiconductor-Insulator-Semiconductor System," *Soviet Physics-Semiconductors*, vol. 11, no. 4, pp. 372–376, 1977.

[4] P. J. Price, "Hot electron effects in heterolayers," *Physica B+C*, vol. 117-118, pp. 750–752, Mar. 1983.

[5] T. J. Gramila, J. P. Eisenstein, A. H. MacDonald, L. N. Pfeiffer, and K. W. West, "Mutual friction between parallel two-dimensional electron systems," *Physical Review Letters*, vol. 66, pp. 1216–1219, Mar. 1991.

[6] A.-P. Jauho and H. Smith, "Coulomb drag between parallel two-dimensional electron systems," *Physical Review B*, vol. 47, pp. 4420–4428, Feb. 1993.

[7] A. G. Rojo, "Electron-drag effects in coupled electron systems," *Journal of Physics-Condensed Matter*, vol. 11, no. 5, p. 31, 1999.

[8] K. Das Gupta, "Transport measurements on electron hole bilayers," 2009.

[9] J. P. Eisenstein, *Course 2 Novel phenomena in double layer two-dimensional electron systems*, vol. 81, pp. 129–176. Elsevier, 2005.

[10] H. Casimir, "On Onsager's Principle of Microscopic Reversibility," *Reviews of Modern Physics*, vol. 17, pp. 343–350, Apr. 1945.

[11] S. Ben-Tabou De-Leon and B. Laikhtman, "Mott transition, biexciton crossover, and spin ordering in the exciton gas in quantum wells," *Physical Review B*, vol. 67, pp. 1–14, June 2003.

[12] B. Laikhtman, "(private communication)."

[13] T. J. Gramila, J. P. Eisenstein, A. H. MacDonald, L. N. Pfeiffer, and K. W. West, "Evidence for virtual-phonon exchange in semiconductor heterostructures," *Physical Review B*, vol. 47, pp. 12957–12960, May 1993.

[14] M. Bø nsager, K. Flensberg, B. Yu-Kuang Hu, and A. H. MacDonald, "Frictional drag between quantum wells mediated by phonon exchange," *Physical Review B*, vol. 57, pp. 7085–7102, Mar. 1998.

[15] M. Kellogg, J. P. Eisenstein, L. N. Pfeiffer, and K. W. West, "Evidence for 2kF electronelectron scattering processes in Coulomb drag," *Solid State Communications*, vol. 123, pp. 515–519, Sept. 2002.

[16] A. Yurtsever, V. Moldoveanu, and B. Tanatar, "Many-body effects in the Coulomb drag between low density electron layers," *Solid State Communications*, vol. 125, pp. 575–579, Mar. 2003.

[17] R. Pillarisetty, H. Noh, D. C. Tsui, E. P. De Poortere, E. Tutuc, and M. Shayegan, "Frictional Drag between Two Dilute Two-Dimensional Hole Layers," *Physical Review Letters*, vol. 89, p. 16805, June 2002.

[18] R. Pillarisetty, H. Noh, E. Tutuc, E. P. De Poortere, K. Lai, D. C. Tsui, and M. Shayegan, "Coulomb drag near the metal-insulator transition in two dimensions," *Physical Review B*, vol. 71, pp. 1–5, Mar. 2005.

[19] U. Sivan, P. M. Solomon, and H. Shtrikman, "Coupled electron-hole transport," *Physical Review Letters*, vol. 68, pp. 1196–1199, Feb. 1992.

[20] H. Rubel, E. H. Linfield, D. A. Ritchie, K. M. Brown, M. Pepper, and G. A. C. Jones, "Study of the carrier density dependence of the frictional drag between closely spaced two-dimensional electron gases," *Semiconductor Science and Technology*, vol. 10, no. 9, p. 1229, 1995.

[21] J. A. Seamons, C. P. Morath, J. L. Reno, and M. P. Lilly, "Coulomb Drag in the Exciton Regime in Electron-Hole Bilayers," *Physical Review Letters*, vol. 102, no. 2, pp. 026804 – 026804–4, 2009.

[22] A. F. Croxall, K. Das Gupta, C. A. Nicoll, M. Thangaraj, H. E. Beere, I. Farrer, D. A. Ritchie, and M. Pepper, "Anomalous Coulomb Drag in Electron-Hole Bilayers," *Physical Review Letters*, vol. 101, no. 24, pp. 246801 – 246801–4, 2008.

[23] A. F. Croxall, K. Das Gupta, C. A. Nicoll, I. Farrer, H. E. Beere, D. A. Ritchie, and M. Pepper, "Towards the ground state of an electronhole bilayer," *Physica E: Low-dimensional Systems and Nanostructures*, vol. 42, pp. 1247–1250, Feb. 2010.

[24] E. H. Hwang and S. Das Sarma, "Transport and drag in undoped electron-hole bilayers," *Physical Review B*, vol. 78, Aug. 2008.

[25] Y. Joglekar, A. Balatsky, and M. P. Lilly, "Excitonic condensate and quasiparticle transport in electron-hole bilayer systems," *Physical Review B*, vol. 72, Nov. 2005.

[26] G. Bastard, *Wave Mechanics Applied to Semiconductor Heterostructures*. Paris: Les Editons de Physique, 1988.

[27] R. S. Knox, *Theory of Excitons*. Academic Press Inc.,U.S., 1963.

[28] Y. Takahashi, Y. Kato, S. S. Kano, S. Fukatsu, Y. Shiraki, and R. Ito, "The effect of electric field on the excitonic states in coupled quantum well structures," *Journal of Applied Physics*, vol. 76, no. 4, p. 2299, 1994.

[29] S. Glasberg, H. Shtrikman, and I. Bar-Joseph, "Optical generation of spatially separated electron and hole gases in intrinsic GaAs/AlxGa1-xAs double quantum wells," *Physical Review B*, vol. 63, Feb. 2001.

[30] B. E. Kane, J. P. Eisenstein, W. Wegscheider, L. N. Pfeiffer, and K. W. West, "Separately contacted electron-hole double layer in a GaAs/AlxGa1xAs heterostructure," *Applied Physics Letters*, vol. 65, no. 25, p. 3266, 1994.

[31] M. Stern, *Optical Spectroscopy of Interacting Electrons and Holes in Coupled Quantum Wells*. Ph.d thesis, Weizmann Institute of Science, 2008.

[32] V. L. Rideout, "A review of the theory and technology for ohmic contacts to group IIIV compound semiconductors," *Solid-State Electronics*, vol. 18, pp. 541–550, June 1975.

[33] T. C. Shen, G. B. Gao, and H. Morkoc, "Recent developments in ohmic contacts for III-V compound semiconductors," *Journal Of Vacuum Science And Technology B*, vol. 10, no. 5, pp. 2113–2132, 1992.

[34] M. Szymanska and P. Littlewood, "Excitonic binding in coupled quantum wells," *Physical Review B*, vol. 67, May 2003.

[35] A. Alexandrou, J. Kash, E. Mendez, M. Zachau, J. Hong, T. Fukuzawa, and Y. Hase, "Electric-field effects on exciton lifetimes in symmetric coupled GaAs/Al0.3Ga0.7As double quantum wells," *Physical Review B*, vol. 42, pp. 9225–9228, Nov. 1990.

[36] S. Ben-Tabou de Leon and B. Laikhtman, "Exciton-exciton interactions in quantum wells: Optical properties and energy and spin relaxation," *Physical Review B*, vol. 63, Mar. 2001.

[37] L. Vina, E. Mendez, W. Wang, L. Chang, and L. Esaki, "Stark shifts in GaAs/GaAlAs quantum wells studied by photoluminescence spectroscopy," *Journal of Physics C: Solid State Physics*, vol. 20, p. 2803, 1987.

[38] J. Golub, K. Kash, J. Harbison, and L. Florez, "Long-lived spatially indirect excitons in coupled GaAs/AlxGa1-xAs quantum wells," *Physical Review B*, vol. 41, pp. 8564–8567, Apr. 1990.

[39] C. Schindler and R. Zimmermann, "Analysis of the exciton-exciton interaction in semiconductor quantum wells," *Physical Review B*, vol. 78, July 2008.

[40] R. Zimmermann and C. Schindler, "Exciton-exciton interaction in coupled quantum wells," *Solid State Communications*, vol. 144, pp. 395–398, Dec. 2007.

[41] D. Snoke, "Predicting the ionization threshold for carriers in excited semiconductors," *Solid State Communications*, vol. 146, pp. 73–77, Apr. 2008.

[42] B. Laikhtman, "(private communication)," 2011.

[43] A. L. Efros, "Metal-non-metal transition in heterostructures with thick spacer layers," *Solid State Communications*, vol. 70, no. 3, pp. 253–256, 1989.

[44] Y. Meir, "Percolation-Type Description of the Metal-Insulator Transition in Two Dimensions," *Phys. Rev. Lett.*, vol. 83, pp. 3506–3509, Oct. 1999.

[45] Y. Meir, "Two-species percolation and scaling theory of the metal-insulator transition in two dimensions," *Physical Review B*, vol. 61, pp. 16470–16476, June 2000.

[46] G. Finkelstein, H. Shtrikman, and I. Bar-Joseph, "Optical Spectroscopy of a Two-Dimensional Electron Gas near the Metal-Insulator Transition," *Physical Review Letters*, vol. 74, no. 6, pp. 976–979, 1995.

[47] A. L. Efros and B. I. Shklovskii, "Coulomb gap and low temperature conductivity of disordered systems," *Journal of Physics C: Solid State Physics*, vol. 8, no. 4, p. L49, 1975.

[48] E. Shimshoni, "Coulomb drag at the onset of Anderson insulators," *Physical Review B*, vol. 56, pp. 13301–13305, Nov. 1997.

[49] M. Stern, V. Garmider, V. Umansky, and I. Bar-Joseph, "Mott Transition of Excitons in Coupled Quantum Wells," *Physical Review Letters*, vol. 100, pp. 1–4, June 2008.

[50] Y. Hanein, D. Shahar, J. Yoon, C. Li, D. Tsui, and H. Shtrikman, "Properties of the apparent metal-insulator transition in two-dimensional systems," *Physical Review B*, vol. 58, pp. R7520–R7523, Sept. 1998.

מכון ויצמן למדע

WEIZMANN INSTITUTE OF SCIENCE

Thesis for the degree
Master of Science

Submitted to the Scientific Council of the
Weizmann Institute of Science
Rehovot, Israel

עבודת גמר (תזה) לתואר
מוסמך למדעים

מוגשת למועצה המדעית של
מכון ויצמן למדע
רחובות, ישראל

By
**Yuval Vardi**

מאת
יובל ורדי

# זרם גרר של אלקטרונים וחורים מעוררים אופטית בשתי שכבות בבורות קוונטיים מצומדים

# Coulomb Drag in an Optically Generated Electron-Hole Bilayer

Advisor:
Prof. Israel Bar-Joseph

מנחה:
פרופ' ישראל בר-יוסף

January 2011

שבט תשע"א